# New Precursors Derived Activated Carbon and Graphene for Aqueous Supercapacitors with Unequal Electrode Capacitances

CHEN Yao [1,*], CHEN George Zheng [1,2,3,*]

[1] The State Key Laboratory of Refractories and Metallurgy, College of Materials and Metallurgy, Wuhan University of Science and Technology, Wuhan 430081, P. R. China.

[2] Department of Chemical and Environmental Engineering, Faculty of Science and Engineering, University of Nottingham Ningbo China, Ningbo 315100, Zhejiang Province, P. R. China.

[3] Department of Chemical and Environmental Engineering, Faculty of Engineering, University of Nottingham, Nottingham NG2 7RD, UK.

**Abstract:** Carbon materials can offer various micro- and nano-structures, and bulk and surface functionalities, and hence remain most popular for manufacturing supercapacitors. This article reviews critically recent development in preparation of carbon materials from new precursors for supercapacitors. Typical examples are activated carbon (AC) and graphene which can be prepared from various conventional and new precursors, such as biomass, polymers, graphite oxide, $CH_4$ and even $CO_2$, via innovative processes to achieve low cost and/or high specific capacitance. Specifically

---

Received: April 3, 2019; Revised: May 17, 2019; Accepted: May, 2019; Published online: May, 2019.

[*] Corresponding authors. Email: y.chen@wust.edu.cn (C.Y.); george.chen@nottingham.ac.uk (C.Z.).

The project was supported by the State Key Laboratory of Materials Processing and Die & Mould Technology, Huazhong University of Science and Technology, China (P2019-014) and Ningbo Municipal Government, China (3315 Plan, and 2014A35001-1).
华中科技大学材料成形与模具技术国家重点实验室开放基金(P2019-014)、宁波市政府(3315 划和 2014A35001-1)资助项目

for making AC from natural biomasses or synthetic polymers, either new, spent or waste, the popular activation agents, such as KOH and $ZnCl_2$, are often used to process the ACs derived from these new precursors, whilst the respective activation mechanisms always attract interests. The traditional two-step calcination process at high temperatures is widely employed to achieve high performance, with or without retaining the morphology of the precursors. The three-step calcination, including a post-vacuum treatment, is also the choice in many cases, but it can increase the cost per capacity ($kWh \cdot g^{-1}$). The more recently reported one-step molecular activation promises a better and more economical approach to the commercial application of AC, although further increase of the yield is necessary. In addition to activation, graphitization, N doping and template control can further improve ACs in terms of the charging and discharging rates, or pseudocapacitance, or both. Considerations are also given to material structure design, and carbon regeneration during activation. Metal-organic frameworks which were initially used as templates are found to be good direct carbon precursors. Various structures of graphene, including powders, films, aerogels, foams and fibers, can be produced from graphite oxide, $CO_2$ and $CH_4$. Similar to AC, graphene can possess micropores by activation. Self-propagating high temperature synthesis and molten salt processing are newly reported methods for fabrication of mesoporous graphene. Macroporous graphene hydrogels can be produced by hydrothermal treatment of graphite oxide suspension, which can also be transferred into films. Hierarchically porous structures can be achieved by $H_2O_2$ etching or $ZnCl_2$ activation of the macroporous graphene precursor. Sponges as templates combining with KOH

activation are applied to create both micro- and macropores in graphene foams. Graphene can grow on fibers and textiles by electrodeposition, dip-coating or filtration, which can be woven into clothes with a large area or thick loading, illuminating the potential application in flexible and wearable supercapacitors. The key restrictions on production of AC and graphene are high cost, low yield, low packing density and low working potential range. Most of the new precursors derived carbon materials work very well with aqueous electrolytes, whilst charge storage occurs not only in the electric double layer (i.e. the “carbon | electrolyte” interface), but also via redox activity in association with the bulk and surface functionalities, and the resulting partial delocalization of valence electrons. The analysis of the capacitive electrode has shown a design defect that prevents the working voltage of a symmetrical supercapacitor from reaching the full potential window of the carbon material. This defect can be avoided in AC based supercapacitors with unequal electrode capacitances, leading to higher cell voltages and hence higher specific energy than that of their symmetrical counterparts. There are also emerging ways to raise the energy capacity of AC supercapacitors, such as the use of redox electrolytes to enable the Nernstian charge storage mechanism, and of the 3D printing method for a desirable electrode structure. All these progresses are promising carbon materials from various precursors of new and waste sources for a more affordable and sustainable supercapacitor technology.

Key Words: New precursors; Activated carbon; Graphene; Aqueous supercapacitor; Unequal electrode capacitances.

# 新碳源制备活性炭和石墨烯及其非等电极电容水系超级电容器

陈尧 [1,*]，陈政 [1,2,3,*]

[1] 武汉科技大学，省部共建耐火材料与冶金国家重点实验室，材料与冶金学院，武汉 430081

[2] 宁波诺丁汉大学，科学与工程学院，化学与环境工程系，浙江宁波 315100

[3] 诺丁汉大学，工程学院，化学与环境工程系，英国诺丁汉 NG2 7RD

**摘要：**碳材料具有不同的微米和纳米结构以及本体和表面的官能基团，因此成为最普遍采用的超级电容器电极材料。典型的例子是活性炭和石墨烯。最近的研究趋势是通过新方法，以传统和新碳源，例如生物质、聚合物、氧化石墨、碳氢以及二氧化碳气体，来制备成本低、电容性能高的活性炭和石墨烯。特别是，大多数新碳源衍生碳非常适用于水系电解液。电荷存储不仅发生在“碳|电解液”界面上（形成双电层），也依靠本体和表面的官能化带来的氧化还原活性，包括有限离域价电子转移反应。此外，进一步理解电荷存储机制有助于设计出比传统对称电容器具有更高电压和比能量的非等电极电容水系超级电容器。本文综述了新碳源衍生碳材料和器件的最新进展，为超级电容器技术的持续发展助力。

**关键词：新碳源；活性炭；石墨烯；水系电容器；非等电极电容**

**中图分类号：**O646

**Biography**

Yao Chen

Yao Chen (ORCID: 0000-0003-0147-8156) obtained his PhD degree from Institute of Electrical Engineering, Chinese Academy of Science under Prof Yanwei Ma's supervision in 2012. He then completed his postdoc research in IFW Dresden, Germany, together with Prof. Oliver Schmidt and in AIST Kansai, Japan with Prof. Qiang Xu. Since 2015, as an instructor, he had joined Wuhan University of Science and Technology where he was mainly engaged in research on carbon based electrochemical energy storage devices and heterogeneous catalysis.

George Zheng Chen

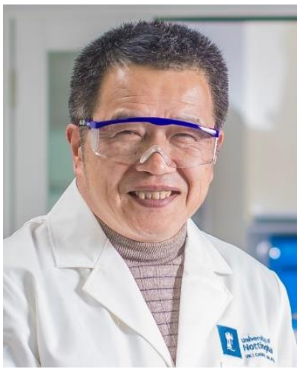

George Z. Chen (ORCID: 0000-0002-5589-5767) graduated from Jiujiang Teachers Training College with a Diploma in 1981, Fujian Normal University with the MSc in

1985, and the University of London with the PhD and DIC in 1992. After contracted work in the Universities of Oxford, Leeds and Cambridge, he joined the University of Nottingham in 2003, and has been Professor since 2009. He is Li Dak Sam Chair Professor of the University of Nottingham Ningbo China, and Specially Invited Professor of Wuhan University of Science and Technology. His research aims at electrochemical and liquid salts innovations for materials, energy and environment with financial supports from various sources, such as the Schlumberger Interdisciplinary Fellowship (Darwin College Cambridge), Cheung Kong Scholarship (MoE of China), Distinguished Young Scholars Fund (NSFC), Brian Mercer Feasibility Award (Royal Society), International Energy Research Award (E.ON AG), REFINE Consortium (EPSRC), and the 3315 Plan for Innovation Team (Ningbo City).

# 1 Introduction

Electrochemical energy storage (EES) technologies are widely applied in personal electronics for many years. Nowadays, the fast increasing depletion of fossil resources and the concomitant environmental pollution further stimulate various research and commercial interests in EES. Fig. 1 shows the Ragone plots of various EES devices in comparison with that of internal combustion engine [1]. Of all these, supercapacitors have unique advantages of higher power capability (comparable to that of internal combustion engines) and longer cycle life than, for example, rechargeable lithium ion batteries and redox flow batteries. However, it is desirable to obtain higher specific energy for the supercapacitors. According to the charge storage mechanisms, supercapacitors are divided into two categories: electrical double layer (EDL) capacitors and pseudocapacitors. The EDL capacitors based on carbon materials with high specific surface area (SSA) store electric energy by potential-dependent accumulation of electric charges from reversible adsorption of ions of the electrolyte onto the carbon/electrolyte interface to form the EDL within the porous carbon electrode. Taking a carbon negative electrode (negatrode) as an example, as revealed by Fig. 2, the EDL in fact has a multi-layer structure, including the inner compact layer, outer compact layer and diffuse layer which is next to the bulk electrolyte solution [1]. Partially or fully desolvated ions exist in the compact layer. The specific capacitance of the EDL capacitor is roughly in proportion to the electrolyte ion accessible SSA of the carbon electrode. Pseudocapacitors rely on reversible faradaic (or redox) reactions in the active electrode materials, typically including transition metal oxides, metal hydroxides and conducting polymers [2]. The specific capacitances of pseudocapacitors are greater than those of EDL capacitors due to faradic reactions storing charges at the atomic or molecular levels. However, repeated expansion and contraction also occur in the electrode materials of pseudocapacitors during charge-discharge cycling. These are due to the ingression and egression of counter ions to maintain electric neutrality in the electrode materials, in response to the faradic reactions, leading to the well-known poor cycle lives of pseudocapacitors [3]. Similarly, the faradaic reaction caused expansion and contraction cycles and the consequent detriments also occur when charging-discharging lithium ion batteries repeatedly. Considering the advantages of high power capability, good cycle life and low cost, activated carbons (ACs) are currently the most popular commercial electrode materials.

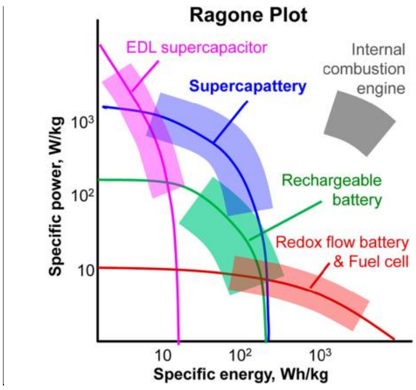

Fig. 1 Ragone plots for various electrochemical energy storage devices in comparison with internal combustion engines [1].

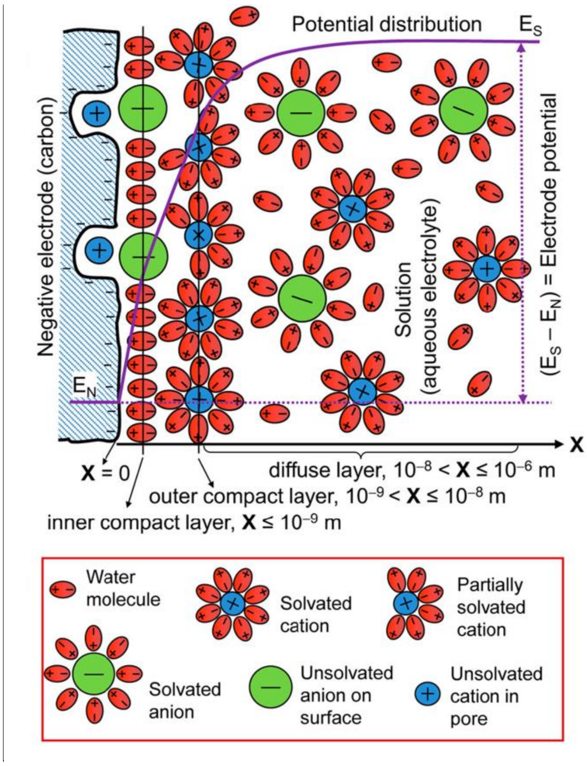

Fig. 2 Schematic representations of the EDL structure of the interface between a porous carbon negatrode and an aqueous electrolyte [1].

ACs are commonly derived by carbonization of carbon-rich precursors at high temperatures in an inert atmosphere and subsequent activation. In practices, KOH, $H_3PO_4$ and $ZnCl_2$ are often used as the activating agents for chemical activation, while $CO_2$ and water steam for physical activation. The chemical activation procedures leave behind the combination of the disordered microporous and mesoporous structures in ACs by etching the carbonized specimens with these activating agents at high temperature. Therefore, ACs can possess typically the Brunauer-Emmett-Teller (BET) measured SSA ranging from 500 to 3000 $m^2 \cdot g^{-1}$ and have specific capacitances of 100 to 300 $F \cdot g^{-1}$ in organic or alkaline aqueous electrolytes, respectively [4-6]. In terms of structure, ACs are usually considered to be non-crystalline, whilst at atomic scales they are mainly composed of disorderly arranged graphene layers with various defects [7]. Thus, the properties of ACs are intrinsically linked to those of graphene.

Isolated and well-structured graphene layers were first reported in 2004, and considered to hold great promises for many applications. Such predictions are based on the fact that monolayer graphene has a very large theoretical SSA of 2630 $m^2 \cdot g^{-1}$, high carrier mobility over 10,000 $cm^2 \cdot V^{-1} \cdot s^{-1}$ and extreme Young's modulus of 1.0 TPa [8-10]. In 2007, chemically converted graphene (called "graphene" for short in this review afterwards) was first prepared by reducing exfoliated graphite oxide (GO) with $N_2H_4 \cdot H_2O$ [11]. Then, graphene has been exploited as the electrode material of supercapacitors [12]. Subsequently, stable dispersions of graphene monolayers were obtained by adjusting pH during the reduction of GO with a suitable amount of $N_2H_4 \cdot H_2O$ [13]. Although experimentally obtained graphenes have SSAs far below the theoretic value, they still show specific capacitances similar to those of ACs, which can be attributed, at least partly, to the partial delocalization of valence electrons in oxygenated graphene according to a recent Density Functional Theory modeling assisted study [14]. In this study, it was found that electron transfer reactions, also known as Faradaic processes, can be undertaken by localized or partially delocalized valence electrons. The former follows the Nernst equation and is featured by peak-shaped cyclic voltammograms (CVs). However, the latter is responsible for the so called pseudocapacitance with the CVs having the same rectangular shape as that of a porous carbon electrode with high specific surface area and hence high EDL capacitance. This understanding explains well the differences between rechargeable battery electrodes which often show peak-shaped CVs and supercapacitor electrodes which are well known for their rectangular CVs.

As revealed in Fig. 1, commercial EDL capacitors based on ACs could have specific energy of about 5 Wh·kg$^{-1}$ for the whole device. Comparing with rechargeable lithium ion batteries, the specific energy of AC based EDL capacitors is not high enough to meet the requirements of some power sources, especially in electric vehicles. The energy capacity ($E$) of a supercapacitor is defined by Equation 1,

$$E = \frac{1}{2}QU = \frac{1}{2}CU^2 \tag{1}$$

where $Q$ is the charge, $C$ is the total capacitance of the cell, and $U$ is the cell voltage which is primarily related to the electrolyte used. The thermodynamic potential window of water is 1.23 V at room temperature, whilst organic electrolytes have higher decomposition voltages (above 2.50 V). Even if the specific capacitance in the organic electrolytes is a half of that in aqueous electrolytes, the energy of a cell in organic electrolytes is still higher because it is proportional to the square of the cell voltage. Nonetheless, organic electrolytes are usually highly flammable, making it more vulnerable when a high voltage is applied, which causes severe safety concerns. As for ionic liquids, their high viscosities at room temperature would induce even slower motion of the large organic ions, making it difficult and slow to access the internal surface of AC and hence very low specific capacitance. Therefore, the advantages of high conductivity and heat capacity, low cost and environmental impact of aqueous electrolytes have stimulated more research towards a breakthrough over the thermodynamic potential window of water. The extension of the cell voltage of an aqueous supercapacitor can be fulfilled by using electrode materials with high over-potentials for evolution of either or both hydrogen and oxygen gases.

In this review, attention is focused on the development in preparation of ACs from different precursors, and of graphenes in various forms in recent years. Then, the mechanism of extending the cell voltage and improving the performance of aqueous supercapacitors are introduced. Further, new trends of making better performing carbon materials for supercapacitors are introduced and discussed.

## 2 Activated carbon

As mentioned in Introduction, ACs are usually prepared by carbonization and subsequent activation steps. Natural materials, such as coconut shells and wood, are firstly selected as the carbon-rich precursors due to their low cost. Of course, synthetic materials can also be the carbon-rich precursors of ACs for specific purposes. A porous network in the body of carbon particles is produced after activation. The International Union of Pure and Applied Chemistry (IUPAC) categorizes pores into micropores (< 2 nm), mesopores (2~50 nm) and macropores (>50 nm) according to their diameters [15]. Generally, all of these can be created, but micropores dominate in carbon grains. If markedly more mesopores are produced during activation, besides micropores, type IV nitrogen adsorption desorption isotherms can be observed. Otherwise, dominated micropores lead to type I isotherms. The most commonly used activating agent is KOH, with which the activation mechanism is governed by the reaction Equation 2.

$$6\mathrm{KOH} + 2\mathrm{C} \triangleq 2\mathrm{K}\uparrow + 3\mathrm{H_2}\uparrow + 2\mathrm{K_2CO_3} \tag{2}$$

Note that Equation 2 is thermodynamically unfavorable at temperatures below 700 °C, but it can proceed if the gaseous products are continuously removed. Particularly, the melting and boiling points of K are 63.38 and 758.85 °C, whilst KOH melts and boils at 360 and 1327 °C, respectively. Thus, even when K is produced at a sufficiently high temperature but below the boiling point, the liquid metal can still reach a sufficiently high vapor pressure and escape from the reaction sites. Comparing with KOH, the activation mechanism of $ZnCl_2$ is more complicated. In the early stage of pyrolysis, $ZnCl_2$ works as a catalyst for the dehydrogenation and dehydration reactions of the precursor, inducing hydrogen evolution [16], charring and aromatization of the carbon, and restricting the formation of tar [17]. We think that the restriction of $ZnCl_2$ evaporation below 600 °C [18] and evolution of methane [16] correspond to the creation of pores in AC.

## 2.1 Activated carbon from biomass

Traditionally, the coconut shells as carbon-rich biomass wastes are the main precursor for the production of ACs. Nowadays, other biomass wastes, such as lignin [19], bagasse [20], loofah sponge [21], willow catkin [22,23], hemp bast fiber [24] and bamboo industrial byproduct [25], can also be used as the carbon sources for making ACs.

Some natural biomass wastes were utilized due to their special microscopic morphology being similar to those of carbon nanotubes or graphene. Researchers expected to maintain the specific morphology during the production of AC in order to utilize more micropores for supercapacitors. For example, loofah sponges could yield ACs which exhibited a three dimensional (3D) network consisting of cross-linked hollow microtubes with wall thickness of around 2 μm [21]. Like carbon nanotubes, willow catkins show a hollow microtubular structure with the diameter of 10 μm and the wall thickness of 1 μm. The conventional two-step method consisting of carbonization at 600 °C for 4 h and activation with KOH by 4 times of mass at 800 °C for 1 h could produce hierarchical porous carbon microtubes, which are helpful for the diffusion of electrolyte ions into the inner micropores. In comparison, a control sample prepared by one-step activation without the carbonization could only exhibit irregular granular aggregates, which is entirely different from the natural tubular morphology of willow catkins [22]. Only the Type I $N_2$ adsorption and desorption isotherms could be observed, suggesting that mesopores were absent in the control sample. The BET SSA and the pore volume of the hierarchical carbon microtubes were 1776 $m^2 \cdot g^{-1}$ and 0.85 $cm^3 \cdot g^{-1}$, respectively. The hierarchical carbon microtubes in 6 $mol \cdot L^{-1}$ KOH electrolyte had a specific capacitance value of 292 $F \cdot g^{-1}$ at 1 $A \cdot g^{-1}$ in a three-electrode cell. The morphology retention by the two-step method is likely because during carbonization at high temperatures, willow catkins should only undergo dehydration without any significant alterations in the carbon skeleton (structure), whilst the follow-on activation could only attack the remaining carbon structure, according to Equation 2. However, in the one step method, the KOH could attack both the willow catkins precursor and its carbonization products at different stages of the process, and hence destroy the original morphology.

Another biomass waste is hemp bast fiber that can be converted to crumpled graphene-like carbon nanosheets [24]. During the fabrication, the hydrothermal treatment of hemp bast fiber in a dilute acid solution at 180 °C for 12 h replaced the conventional carbonization at high temperatures, which could potentially reduce the production cost. The bamboo-based industrial byproduct was also treated by the hydrothermal method in a liquid containing sulfuric acid at 200 °C for 12 h before activation. The final bamboo-derived carbon was subjected to post vacuum annealing at 800 °C for 1 h after activation [25]. The BET SSA of 1472 $m^2{\cdot}g^{-1}$ and the specific capacitance of 301 $F{\cdot}g^{-1}$ (in 6 $mol{\cdot}L^{-1}$ KOH in a three-electrode cell) were obtained for the three-step treated bamboo-derived carbon. If direct pyrolysis at 800 °C for 2 h was applied instead of the hydrothermal treatment, the control sample possessed 96% micropore volume, giving a slightly lower SSA of 1106 $m^2{\cdot}g^{-1}$. Another control sample without post vacuum annealing also showed a lower specific capacitance, indicative of the importance of the hydrothermal treatment and the post vacuum annealing.

Obviously, not all biomasses have the desired morphology and structure. Instead, new structures to enable specific functionalities are often needed to build from the precursors. For example, gelatin, a biological extractive from animal syndesm, could turn to a honeycomb-like porous structure with glutaraldehyde via cryodesiccation, which gave AC with a maximum BET SSA of 3692 $m^2{\cdot}g^{-1}$ up to date. The specific capacitance of 305 $F{\cdot}g^{-1}$ for a single electrode was obtained in a symmetrical two-electrode cell [26]. Also, opportunities are always sought after to further lower the energy input for AC production. In this line, a new method was developed to achieve molecular level one-step activation to prepare AC with agar as a precursor which is the extractive from seaweed [27]. The dehydration (or deoxygenation) of agar was achieved by dissolving agar in a hot KOH aqueous solution below 100 °C. It was observed that the color of the aqueous solution turned dark black. The increased C/O molar ratio of such treated agar samples was attributed to the removal of hydrogen bonded hydroxyl groups and cyclic ether linkage of six member rings in agar by a dehydration reaction with KOH in the hot solution, as revealed by infrared (IR) spectra (Fig. 3a). Surprisingly, the one-step activation of agar in the subsequent calcination produced an interconnected 3D network with macrovoids of several micrometers with a wall thickness of several hundred nanometers. The control sample processed by the conventional two-step method presented bulk characteristic with fractured large macrovoids, suggesting that the molecular level activation occurred in the one-step calcination (Fig. 3c and d). Therefore, the one-step derived AC possessed a larger SSA of 1672 $m^2 \cdot g^{-1}$ and total pore volume of 0.81 $cm^3 \cdot g^{-1}$ which compare favorably with 1048 $m^2 \cdot g^{-1}$ and 0.47 $cm^3 \cdot g^{-1}$ for the two-step derived AC, respectively. The specific capacitance of the one-step derived AC was 226 $F \cdot g^{-1}$ in a three-electrode cell, 38% higher than that of the two-step derived AC (Fig. 3b). The symmetrical two-electrode cell with an electrolyte of 6 $mol \cdot L^{-1}$ KOH also exhibited a maximum specific capacitance of 57 $F \cdot g^{-1}$ at 0.25 $A \cdot g^{-1}$, corresponding to 228 $F \cdot g^{-1}$ for a single electrode. The improved charge storage performance should be attributed to the unique 3D morphology and pore characteristics whilst the low temperature and high efficiency production is indicative of the commercial potential of the molecular level one-step activation.

Comparing with the conventional two-step method, an extra vacuum post-treatment could increase the capacitive behavior of AC, however, the cost per $kWh \cdot g^{-1}$ is still high. Therefore, molecular one-step activation has a better promise in commercial preparation of AC. The bottleneck to commercial development of the one-step process is the relatively low yield of AC.

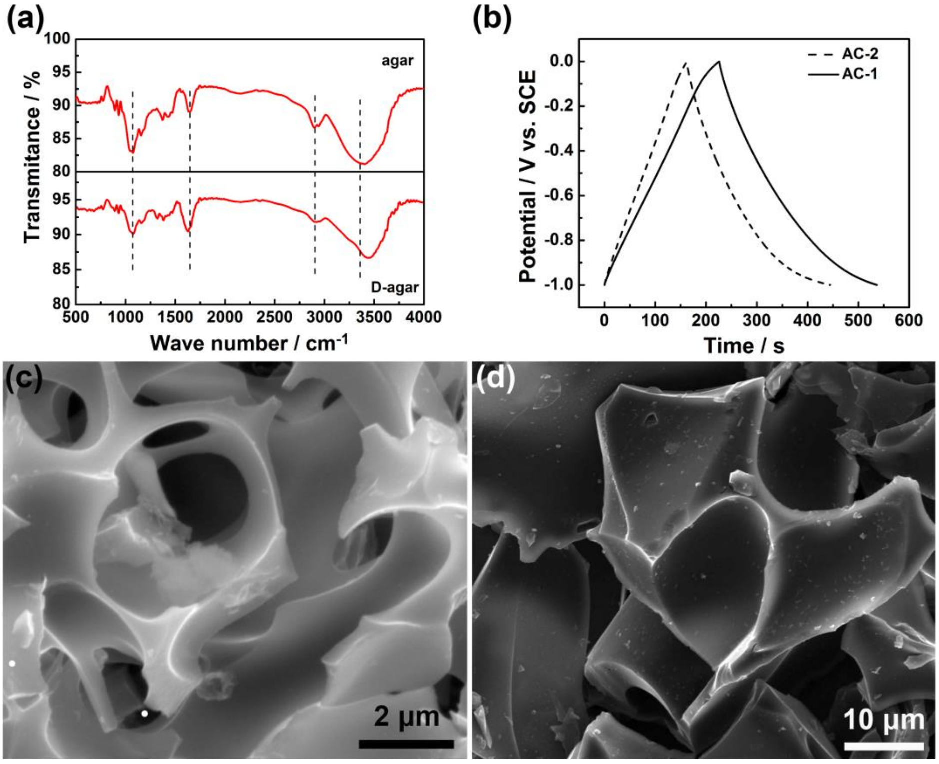

Fig. 3 Molecular level one-step activation of agar. (a) IR spectra of agar and deoxygenated agar (D-agar) resulting from a hot KOH solution. (b) Charge-discharge curves of AC by one-step (AC-1) and conventional two-step (AC-2) method. SEM images of (c) AC-1 and (d) AC-2 [27].

## 2.2 Activated carbon from polymers

Apart from natural biomass, synthetic materials were also used to prepare ACs, aiming at controllable morphology, porosity or component. Phenolic resin is one of the most conventional synthetic materials as the carbon precursor due to its high carbon yield and structure stability. Although other synthetic materials are inferior to phenolic resin in terms of cost and production scale, they also have potential applications in AC industry particularly when they are spent or out of period of validity. A dye intermediate, (2-benzimidazolyl) acetonitrile ($C_9H_7N_3$), could form AC with a high SSA of 2980 $m^2 \cdot g^{-1}$ during the pyrolysis with KOH. However, most of the N element in the precursor was not retained at such a high temperature. The $C_9H_7N_3$-derived AC showed 286 and 221 $F \cdot g^{-1}$ in capacitance at 0.5 $A \cdot g^{-1}$ in 2 $mol \cdot L^{-1}$ KOH and 1 $mol \cdot L^{-1}$ $Na_2SO_4$ electrolyte in the two-electrode cells, respectively [28]. Conductive polymers, for instance polyaniline [29], binders, such as polyvinylidene fluoride (PVDF) [30], polytetrafluoroethylene [31], and dispersants, including polyvinylpyrrolidone [32], were all attempted as carbon precursors. Among these facile synthetic precursors, polyaniline-derived AC showed a high specific capacitance of 455 $F \cdot g^{-1}$ in a three-electrode cell containing 6 $mol \cdot L^{-1}$ KOH, while PVDF-derived AC exhibited a large SSA of 3000 $m^2 \cdot g^{-1}$. Considering that polyaniline could be designed to vertically grow on GO, AC with structure combination of 1 D and 2 D was produced after carbonization and activation, giving a specific surface area of 2416 $m^2 \cdot g^{-1}$ with a total pore volume of 1.88 $cm^3 \cdot g^{-1}$, which is higher than those of polyaniline-derived AC [33].

Additionally, polymers with peculiar molecular structure, such as poly[(pyrrole-2,5-diyl)-co-(benzylidene)] [34] and triazine-based covalent organic polymer [35], were expected to lead to regular-structured ACs as well as hetero-atom doping. However, the nitrogen content in these ACs from complicated N containing co-polymers as precursors were not beyond 5% atomic fraction when they were subjected to higher-temperature activation. Fortunately, morphology could be often retained after carbonization and activation at high temperatures. Interestingly, poly-N-phenylethanolamine (PPEA) yielded AC with peculiar morphology. N-phenylethanolamine (PEA) surrounded with hexadecyltrimethylammonium bromide were polymerized by ammonium peroxydisulfate (APS). The shell of the polymer which was produced at the initial reaction prevented further reaction between APS and the interior PEA, perhaps leaving oligomers of PEA within the shell. Therefore, the PPEA-derived AC showed a peanut-shell-like morphology after one-step activation (Fig. 4) [36]. As a result, a BET SSA of 3103 $m^2 \cdot g^{-1}$ was obtained by activation at 800 °C, corresponding to 356 $F \cdot g^{-1}$ at 1 $A \cdot g^{-1}$ in a three-electrode cell with 1 $mol \cdot L^{-1}$ $H_2SO_4$.

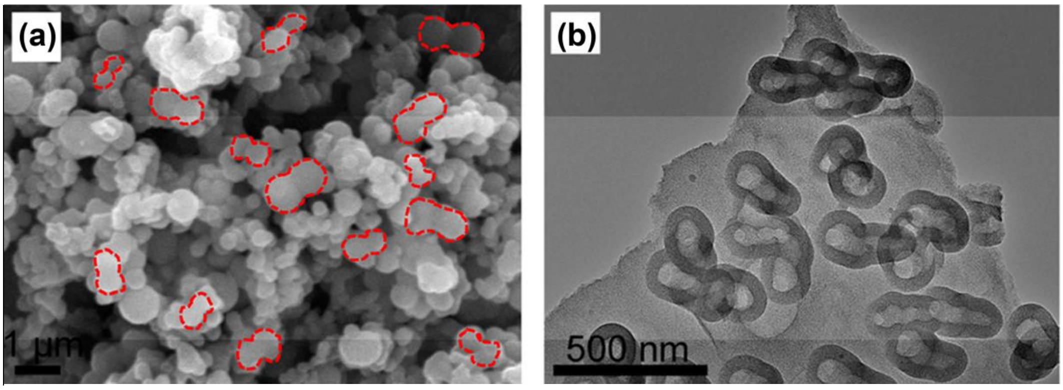

Fig. 4 (a) SEM and (b) TEM images of PPEA-derived AC [36].

Although the cost of synthetic polymers may be high, their spent or waste forms, can be precursors of ACs for special applications. The benefits from using synthetic polymers as the precursor for ACs are the designation of special morphology, structure and even component, which may result in higher performance.

### 2.3 Graphitic activated carbon

Although hemp bast fiber could be converted to crumpled graphene-like carbon nanosheets, the very much desired graphitization in relevance to, for instance, conductivity and structural stability was not observed in the products. In order to give rise to graphitic ACs, a graphitic catalyst precursor of $FeCl_3$ and another activating agent of $ZnCl_2$ were introduced simultaneously into the skeleton of the coconut shell. One-step calcination completed the graphitization with activation only at 900 °C in $N_2$. The transmission electron microscopy (TEM) images in Fig. 5a and b indicate 11 graphene layers in the graphitic AC nanosheets. The graphitization was associated with the transformation from $Fe^{3+}$ ions to carburized phase to Fe at a high temperature, as revealed by the XRD pattern (Fig. 5c). The Fe components could form a carburized phase during the heating process, and decomposition of the carburized phase could lead to the graphitization to form graphene-like nanosheets [37]. The Raman spectrum (Fig. 5d) showed an evident 2D band at 2743 $cm^{-1}$ and a high intensity ratio of the G to D bands, suggesting that the graphitic AC nanosheets were composed of few layers of graphene according to the Raman theory [38]. The BET surface area and total pore volume of the graphitic AC nanosheets were 1874 $m^2 \cdot g^{-1}$ and 1.21 $cm^3 \cdot g^{-1}$. Although the BET SSA of the control sample, non-graphitic AC, reached a higher value of 2007 $m^2 \cdot g^{-1}$, its specific capacitance of 210 $F \cdot g^{-1}$ was lower than 268 $F \cdot g^{-1}$ for the graphitic AC nanosheets as measured in a three-electrode cell. The symmetric two-electrode supercapacitor with the 6 $mol \cdot L^{-1}$ KOH electrolyte had a specific capacitance of 69 $F \cdot g^{-1}$ at 1 $A \cdot g^{-1}$, corresponding to 276 $F \cdot g^{-1}$ for a single electrode, similar to that in the three-electrode cell. These differences were attributed to the high electronic conductivity facilitating the efficient ionic and electronic transport. However, it may also be attributed to the pseudocapacitance resulting from partial delocalization in the more graphitic sample [14].

Another crumpled graphitic carbon nanosheets were prepared by the same method plus a post vacuum annealing with inner shaddock skins as a precursor [39]. Although the macroscopic shape of inner shaddock skins was similar to graphene, the 2D band on the Raman spectrum was not very sharp. It suggests that the graphitization induced formation of graphene was perhaps much more associated with the component than macroscopic shape. However, the $sp^2/sp^3$ ratio doubled comparing with crumpled carbon nanosheets prepared without using $FeCl_3$ as the catalyst.

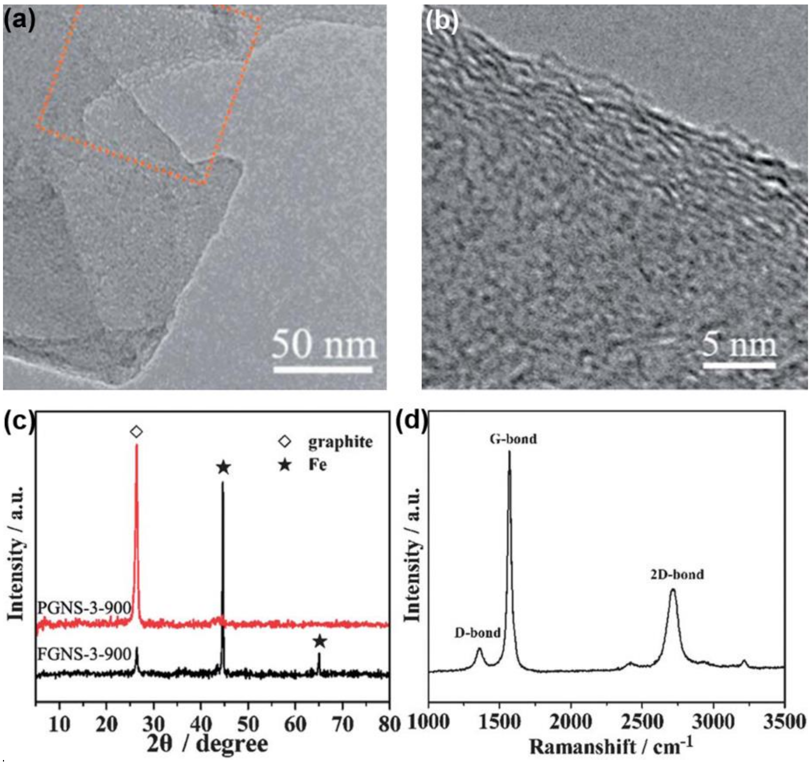

Fig. 5 Graphitization of AC from coconut shell using $FeCl_3$ catalyst. TEM images of the graphitic AC in (a) low and (b) high magnifications. (c) XRD patterns of the graphitic AC before (FGNS-3-900) and after (PGNS-3-900) acid washing. (d) Raman spectrum of the graphitic AC [37].

## 2.4 N doping

It is known that doping with hetero-atoms, for instance N, is an effective strategy to increase the specific capacitance of carbon materials, probably due to the resulting pseudo-capacitance and wettability to electrolytes. $NH_3$ is a commonly used nitrogen source and can be flown into the heat treatment reactor to prepare N-doped ACs. When the corncobs were employed as the precursor, which was mixed with KOH and subjected to the $NH_3$ flow, the nitrogen mass fraction of the N-doped AC increased from 2.97% at 400 °C to 3.98% at 600 °C [40]. However, much increased oxidized pyridinic N was found in the N-doped AC heated at 600 °C, which was considered to have resulted in the capacity drop in the organic $LiPF_6$ electrolyte compared with that at 400 °C.

As mentioned above, phenolic resin is one of the most conventional synthetic materials and can be used as the carbon precursor, particularly when it is spent. The change of components, such as N doping, can be readily fulfilled during the reaction for the synthetic materials. Melamine with a high N content was added to the formaldehyde and resorcinol solution [41]. The slow thermal oxidation at 250 °C in air stabilized the thermoplastic structure and increased the N content. After carbonization and activation, a high N mass fraction of 12.5% and an SSA of 2234 $m^2 \cdot g^{-1}$ were detected in the synthetic N-doped AC. The symmetrical two-electrode cell in 3 $mol \cdot L^{-1}$ $H_2SO_4$ showed a specific capacitance that is equivalent to 309 $F \cdot g^{-1}$ for a single electrode. Similarly, 3,3’-diaminobenzidine could react with *p*-benzoquinone to produce a polymer (PDB) with high N and O contents. Luckily, after pyrolysis with KOH, 11.0% of N and 10.4% of O mass fraction remained in the resulted AC, which showed an SSA of 2660 $m^2 \cdot g^{-1}$ [42]. A specific capacitance of 72.5 $F \cdot g^{-1}$ (290 $F \cdot g^{-1}$ for a single electrode) at 0.2 A·g$^{-1}$ was obtained in a two-electrode cell in 6 mol·L$^{-1}$ KOH, corresponding to a volumetric capacitance of 29.7 F·cm$^{-3}$.

Fresh egg white is a natural nitrogen-rich source. The precipitated protein by ethanol was pyrolyzed at 650 °C for 2 h and further activated at 550 °C for 2 h under an Ar atmosphere [43]. Carbonization and activation at relatively low temperatures in Ar retained 6.5% of N mass fraction. An increased O mass fraction of 16.5% was detected in the sample after activation. High specific capacitances of 556 and 525 F·g$^{-1}$ were measured in three-electrode cells containing 1 mol·L$^{-1}$ $H_2SO_4$ and 1 mol·L$^{-1}$ KOH, respectively. The egg white derived AC as the negatrode was constructed an asymmetrical device with a $NiCo_2O_4$-graphene composite as the positrode, giving 1.55 V in cell voltage and 48 Wh·kg$^{-1}$ in specific energy.

Incorporation of melamine during the preparation of the precursors gave rise to the highest N content among the three examples mentioned above, showing the advantage of making N-doped ACs from precursors with a high N content. Natural nitrogen-rich sources are advantageous in their lower costs and sufficiently high N contents that can be transferred into the produced ACs. Obviously, $NH_3$ annealing is more facile than incorporation of melamine, but the produced AC contained the lowest N content.

### 2.5 Activated carbon with templates

As ZnO presents various morphologies by different synthetic routes and can be readily removed by acid, it is an ideal non-porous template for building hollow structure. For example, ZnO nanorods grown on the Ni foil were utilized as a template to gain hollow Ni arrays by electrodeposition. Subsequent hydrothermal treatment and calcination of glucose and removal of ZnO nanorods induced carbon spheres on hollow Ni arrays [44]. Similarly, flower-like ZnO was fabricated by the reaction between zinc nitrate hexahydrate and trisodium citrate in the NaOH solution. Pitch was coated on the flower-like ZnO and then carbonized and activated. After elimination of the template, the flower-like morphology was maintained for the resulting hierarchical AC which had an SSA of 761.5 $m^2 \cdot g^{-1}$ and a pore volume of 0.49 $cm^3 \cdot g^{-1}$, higher than 375.8 $m^2 \cdot g^{-1}$ and 0.45 $cm^3 \cdot g^{-1}$ respecitively for the control sample, i.e. the flower-like carbon without activation [45]. The symmetric two-electrode supercapacitors in 1 $mol \cdot L^{-1}$ $Na_2SO_4$ had a stable voltage of 1.8 V, delivering a maximum specific energy of 15.9 $Wh \cdot kg^{-1}$.

The MgO powder can also be used as a non-porous template to produce carbon nanolayers by pyrolysis of glucose as the precursor. After KOH activation, the SSA increased from 936 $m^2 \cdot g^{-1}$ for the carbon nanolayers to 2798 $m^2 \cdot g^{-1}$ for the AC nanolayers calculated by the BET theory, arising from hierarchical microporosity and mesoporosity by the chemical activation [46]. Chitosan was used as the precursor in another similar work [47].

Recently, porous MgO was exploited as a template, prepared by calcination of $Mg(OH)_2$ layers formed by boiling MgO powders [48]. Carbonization of coal tar pitch in tetrahydrofuran impregnated into the porous MgO generated pillared-porous carbon on the upper and lower surfaces as well as on the pore walls of the templates [49]. The distance between the two carbon layers was 10~20 nm and the thickness of the individual carbon layer was 2 nm. The mesopores of 6~8 nm were perpendicularly aligned to the surface of the carbon layer.

## 2.6 Activated carbon from metal-organic frameworks

Metal-organic frameworks (MOFs) have well defined nano cavities and open channels, and are ideal templates for making porous carbon materials. Based on this idea, MOF-5 ($Zn_4O(OOCC_6H_4COO)_3$) was initially selected as a microporous template, in which furfuryl alcohol vapor was filled and polymerized. The carbonization of the composite was performed at 1000 °C for 8 h under an Ar flow [50]. ZnO was formed by the decomposition of MOF-5 between 425 and 525 °C and then reduced to Zn metal above 800 °C, which vaporized away at temperatures beyond its boiling point, 908 °C. Carbon species finally was left alone with a BET SSA of 2872 $m^2 \cdot g^{-1}$ and a pore volume of 2.06 $cm^3 \cdot g^{-1}$, showing a specific capacitance of 258 $F \cdot g^{-1}$ at 0.25 $A \cdot g^{-1}$ in a three-electrode cell containing 1 $mol \cdot L^{-1}$ $H_2SO_4$.

When a commercially available MOF sample containing no oxygen, Zeolitic Imidazolate Framework-8 (ZIF-8) was employed as a template to replace MOF-5 [51], it was found that the control sample, ZIF-8 as the only precursor without polymerized furfuryl alcohol, could also yield porous carbon with a SSA of 3148 $m^2 \cdot g^{-1}$. Since then, MOFs as the only precursor and self-template were widely researched. The ZIF-8 directly derived carbon retained a typical crystal morphology which was similar to that of the parent ZIF-8, as shown in Fig. 6. The sample prepared at 900 °C gave a BET SSA of 1075 $m^2 \cdot g^{-1}$ and a specific capacitance of 128 $F \cdot g^{-1}$ in a three-electrode cell using 0.5 $mol \cdot L^{-1}$ $H_2SO_4$ as the electrolyte [52]. It was found that ultrasonication during the synthesis of ZIF-8 could yield an extra small amount of mesopores and macropores.

The sonicated ZIF-8 derived carbon had a BET SSA of 1955 $m^2 \cdot g^{-1}$ and a pore volume of 1.21 $cm^3 \cdot g^{-1}$. After activation with KOH, the SSA of the sonicated ZIF-8 derived AC increased to 2972 $m^2 \cdot g^{-1}$ and the pore volume to 2.56 $cm^3 \cdot g^{-1}$. The specific capacitance of the sonicated ZIF-8 derived AC was 211 $F \cdot g^{-1}$ at 10 $mV \cdot s^{-1}$ for a single electrode, which was higher than 170 $F \cdot g^{-1}$ for the ZIF-8 derived AC without sonication and 158 $F \cdot g^{-1}$ for the sonicated ZIF-8 derived carbon without activation in a two-electrode cell containing 1 $mol \cdot L^{-1}$ $H_2SO_4$ [53]. The increased performance was attributed to extra hierarchical pores produced in ZIF-8 via ultrasonication. However, when $MnO_2$ was redox deposited on sonicated ZIF-8 derived porous carbon materials which were reacted with $KMnO_4$ at room temperature, the specific capacitance of $MnO_2$-inactivated carbon was higher than that of $MnO_2$-AC, which was considered to be due to the hierarchical porous structure in $MnO_2$-inactivated carbon [54]. Additionally, ZIF-8 particles with uniform sizes were synthesized as the precursors by cooling the reactants of $Zn^{2+}$ and 2-methylimidazole before reaction [55].

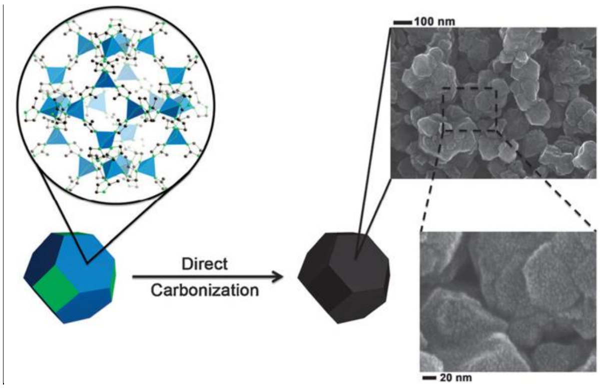

Fig. 6 Scheme of direct carbonization of ZIF-8 to produce the Z-900 carbon sample and its SEM images [52].

Further, the perfect copy on the morphology from MOF precursors to ACs had been demonstrated by strong evidence when MOF-74 rods were used as the precursor. MOF-74 can be made into rod shapes in the presence of salicylic acid as a modulator. The pyrolysis of the rod shaped MOF-74 could form carbon nanorods, proving the maintenance of the morphology. Surprisingly, upon ultrasonication and activation with KOH, the carbon nanorods were transferred to six-layered graphene nanoribbons. The $N_2$ sorption analysis for the graphene nanoribbons showed a typical type II isotherm with an SSA of 1492 $m^2 \cdot g^{-1}$. The specific capacitance of the graphene nanoribbons was 168 $F \cdot g^{-1}$ at 1 $A \cdot g^{-1}$ for a single electrode as derived from the measurement in a two-electrode cell containing 1 $mol \cdot L^{-1}$ $H_2SO_4$ [56]. It was found that the formation mechanism of graphene nanoribbons from carbon nanorods was similar to that from oxygenation of carbon nanotubes [57], which also thanked to maintenance of the rod shape from the MOF precursors.

Table 1 summarized the fabrication of ACs using different precursors and their performance for aqueous supercapacitors in this section.

Table 1 Fabrications and performances of ACs for aqueous supercapacitors.

| **Precursors** [Ref.] | **Activation Reagents** | **Step Number** [a] | **Surface area ($m^2 \cdot g^{-1}$)** | **Electrolyte** | **Current load ($A \cdot g^{-1}$)** | **Capacitance ($F \cdot g^{-1}$)** |
|---|---|---|---|---|---|---|
| **Coconut shell** [37] | $ZnCl_2$+$FeCl_3$ | 1 | 1874 | 6 $mol \cdot L^{-1}$ KOH | 1 | 276 [b] |
| **Agar** [27] | KOH | 1 | 1672 | 6 $mol \cdot L^{-1}$ KOH | 0.25 | 228 [b] |
| **$C_9H_7N_3$** [28] | KOH | 1 | 2980 | 1 $mol \cdot L^{-1}$ $Na_2SO_4$ | 0.5 | 221 [b] |
| **PDB** [42] | KOH | 1 | 2660 | 6 $mol \cdot L^{-1}$ KOH | 0.2 | 290 [b] |
| **Gelatin** [26] | KOH | 2 | **3692** | 6 $mol \cdot L^{-1}$ KOH | 0.5 | 305 [b] |
| **Sonicated ZIF-8** [53] | KOH | 2 | 2972 | 1 $mol \cdot L^{-1}$ $H_2SO_4$ | 10 $mV \cdot s^{-1}$ | 211 [b] |
| **MOF-74** [56] | KOH | 2 | 1492 | 1 $mol \cdot L^{-1}$ $H_2SO_4$ | 1 | 168[b] |
| **Resin+Melamine** [41] | KOH | 3 | 2234 | 3 $mol \cdot L^{-1}$ $H_2SO_4$ | 0.1 | 309[b] |
| **ZIF-8** [52] | — | 1 | 1075 | 0.5 $mol \cdot L^{-1}$ $H_2SO_4$ | 50 $mV \cdot s^{-1}$ | 128 |
| **PPEA** [36] | KOH | 1 | 3103 | 1 $mol \cdot L^{-1}$ $H_2SO_4$ | 1 | 356 |

| | | | | | | |
|---|---|---|---|---|---|---|
| **Willow catkin** [22] | KOH | 2 | 1776 | 6 $\mathrm{mol \cdot L^{-1}}$ KOH | 1 | 292 |
| **Pitch** [45] | KOH | 2 | 762 | 6 $\mathrm{mol \cdot L^{-1}}$ KOH | 2 $\mathrm{mV \cdot s^{-1}}$ | 294 |
| **Egg white** [43] | KOH | 2 | 1217 | 1 $\mathrm{mol \cdot L^{-1}}$ KOH | 0.25 | 525 |
| **Bamboo** [25] | KOH | 3 | 1472 | 6 $\mathrm{mol \cdot L^{-1}}$ KOH | 0.1 | 301 |

[a] Number of Step carried out above 110 °C. [b] Corresponding specific capacitance for a single electrode in the two-electrode cell, without [b] in the three-electrode cell.

## 3 Graphene

Stable dispersions of graphene monolayers were revealed by AFM, signifying a breakthrough in fabrication of graphene from the exfoliated GO. The stable dispersions of graphene could form graphene films by vacuum filtration[13]. The graphene film can be a supercapacitor electrode directly without any binders and conductive additives. In order to facilitate the electrolyte permeation within the tight structure of the film, the electrolyte was pre-incorporated into the electrode before the desiccation of the film [58]. Besides the 2D film form in macrograph, two categories of 3D graphene networks with macropores were prepared. One of these is the graphene hydrogel prepared by the hydrothermal treatment of GO in a static state [59] and the other is the graphene foam by chemical vapor deposition (CVD) on the Ni foam as a template [60]. Additionally, graphene fibers were also fabricated by an injection [61] or casting-like [62] method.

### 3.1 Powders

Large scale production of graphene powders with few layers would be possible by the reduction of GO in aqueous colloids or in furnaces. For liquid reduction, different reducing agents were attempted to reduce GO, such as $N_2H_4$ $H_2O$ [11], $NaBH_4$ [63], NaOH [64], hydroquinone [65], p-phenylene diamine [66], vitamin C [67], HBr [68] and HI [69]. The most popular method to produce the stable graphene dispersions consisting of monolayers is reduction of GO colloids with $N_2H_4$ $H_2O$ as the reducing agent in an ammonia-adjusted pH environment [13]. Rapid annealing in an inert atmosphere could also reduce solid GO powders to few-layer graphene with a lower level of residual oxygen [70]. In order to prevent the restack of graphene after annealing, $Mg(OH)_2$ powders were used to be templates to obtain the graphene sheets with distinctly crumpled morphology (Fig. 7) [71]. The furnace technology could make microporous graphene with a high SSA upon KOH activation [72], following the same mechanism as that for activation of ACs [73]. Mesoporous graphene powders were prepared with $SnO_2$ deposited on GO. The $SnO_2$ acted as catalysts for carbon gasification, yielding perforations 5~10 nm in size on the mesoporous graphene nanosheets (Fig. 8) [74].

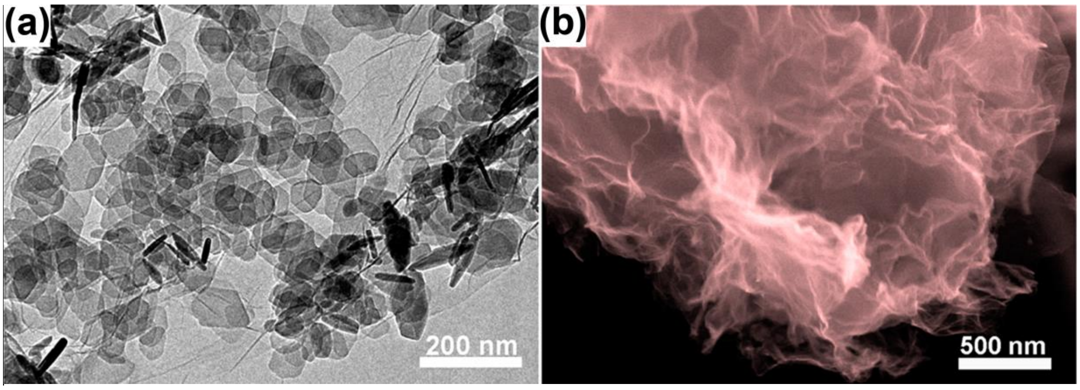

Fig. 7 (a) TEM image of $Mg(OH)_2$ on GO, (b) SEM image of crumpled graphene after removing $Mg(OH)_2$ template [71].

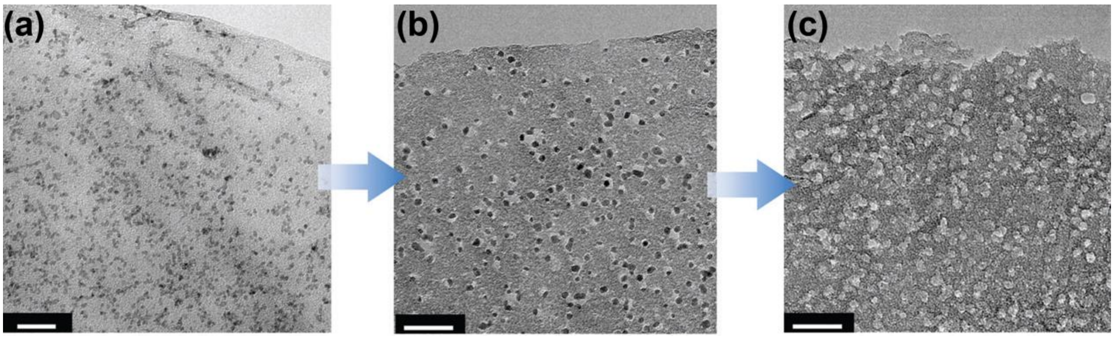

Fig. 8 TEM images of (a) $SnO_2$ on GO, (b) the medium after $SnO_2$ on GO being subjected to controlled air oxidation (c) final mesoporous graphene nanosheets after removing $SnO_2$. Scale bars, 10 nm [74].

Recently, a self-propagating high temperature synthesis (SHS) technology was designed to fabricate scalable mesoporous graphene [75] based on the magnesiothermic reaction, which could be expressed as Equation 3 [76,77].

$$\mathrm{Mg} + \mathrm{CO_2} \triangleq \mathrm{MgO} + \mathrm{C} \qquad (3)$$

A current of 3 A passing through the tungsten coil embedded in the mixture of Mg and MgO for only 5 s created a combustion wave. The excited energy ignited Mg powders in a sealed $CO_2$ atmosphere to trigger the SHS course, during which MgO acted as spacers to prevent the restack of graphene [75]. The SHS-made graphene had an SSA of 709 $m^2 \cdot g^{-1}$ with unimodal pore distribution at 4 nm which was consistent with the size of the MgO template. 98% of $sp^2$ hybridization occupied the SHS-made graphene, resulting in high electrical conductivity of 13000 $S \cdot m^{-1}$, which should be beneficial to achieving high power supercapacitors. As SHS is a furnace technology with low cost due to the very short heat impulse, it promises a high potential for commercialization of graphene once the layer numbers could be further decreased during the SHS.

Besides $CO_2$, carbon nanodot could be another new precursor to prepare macroporous graphene. A 40 W $CO_2$ laser was also applied to irradiate thermolyzed carbon nanodots at low temperature using a laser engraver. Laser irradiation induced a decarboxylation of the upper lying carbon nanodots and released gases, enabling the formation of graphene with spongy micron porous structure [78].

Building pores on graphene basal planes by activation or catalytic oxidation could increase specific capacitance of graphene materials, however, it also brought about materials with low density, which direct resulted in low volumetric capacitance of graphene and consumed superfluous electrolyte. Further, extra electrolyte would increase the weight of the supercapacitor, leading to a low specific energy for the whole device. Molten salt methodology, a metallurgical electrochemistry technology, was developed to fabricate electrode materials in electrochemical energy storage. Treatment of graphene in $NaNH_2$ molten salt simultaneously achieved densification and perforation effects, producing a high packing density of 1.2 $g\cdot cm^{-3}$ for the electrode and 3~5 nm pores on graphene basal planes [79]. The molten salt treated graphene delivered a specific capacitance of 435 $F\cdot g^{-1}$ and a volumetric capacitance of 522 $F\cdot cm^{-3}$ at 1 $A\cdot g^{-1}$ in 6 $mol\cdot L^{-1}$ KOH electrolyte in a three-electrode cell. It is worth noting that the volumetric capacitance of the molten salt treated graphene is 5.4 times as that of untreated graphene, which unveiled the application potential of molten salt methodology for supercapacitors.

### 3.2 Films and aerogels

Graphene films could be prepared via vacuum filtration of stable dispersions, having an outstanding tensile modulus. They can be directly used as electrode without binder and conductive additive. Some graphene composite films were also made via vacuum filtration of the dispersion of graphene composites. A slightly different example was a graphene film that was intercalated with $MnO_2$ on carbon sphere. $MnO_2$ was produced on etched carbon sphere between the interlayer of graphene films using $KMnO_4$ as an oxidant, giving 66.3% of the $MnO_2$ in the composite films [80]. The specific capacitance was 319 $F\cdot g^{-1}$ at 1 $A\cdot g^{-1}$ as measured in a three-electrode cell in 1 $mol\cdot L^{-1}$ $Na_2SO_4$.

After 5000 cycles at 5 $A\cdot g^{-1}$, 94% of the initial capacitance retained. These results indicate a synergistic effect from both the pseudocapacitive and EDL capacitive storage mechanisms in the same material.

A graphene aerogel with an interconnected 3D macroporous network was discovered in the course of the hydrothermal processing and subsequent cryodesiccation [59]. In order to establish mesopores in the graphene aerogel, $H_2O_2$ was employed during the hydrothermal course to partially oxidize and etch the carbon atoms on the more active defect sites of GO. Compressing the holey graphene hydrogel before cryodesiccation produced the holey graphene film [81], which had an SSA of 810 $m^2\cdot g^{-1}$, which was much higher than 260 $m^2\cdot g^{-1}$ for the aerogel without oxidation by $H_2O_2$. The electrolytes were integrated before compression of the holey graphene hydrogel. The holey graphene film with pre-integrated 6 $mol\cdot L^{-1}$ KOH electrolyte had a specific capacitance of 310 $F\cdot g^{-1}$ as derived from measurements in a two-electrode cell.

A pristine GO hydrogel could be obtained by adding a small amount of HCl to the GO dispersion until the pH value reached 0.65 [82]. The GO hydrogel was paved on a glass substrate by blade-casting. The graphene film was obtained by reducing the spread GO hydrogel in a mixed solution of HI and $CH_3COOH$ [83]. The GO hydrogel derived graphene film with a thickness of 388 μm exhibited a high tensile strength of 1 MPa, affording 400 g weights. The areal capacitance of the film was 71 $mF\cdot cm^{-2}$ at 1 $mA\cdot cm^{-2}$ as measured in a two-electrode cell with 1 $mol\cdot L^{-1}$ $H_2SO_4$.

$ZnCl_2$ was found to be an activating agent to tune microporous structure in the graphene aerogel without pulverization. The graphene hydrogel was soaked in the

$ZnCl_2$ solution. After being subjected to vacuum drying and annealing for 1 h under Ar, the microporous graphene aerogel still retained the columnar morphology (Fig. 9) [84]. The activation temperature of 600 °C induced the formation of micropores and simultaneously maintained the bulk density with the highest efficiency. The remaining columnar structure with higher bulk density suggested that $ZnCl_2$ could be a relatively mild activating agent, compared with KOH, which could help balance between the maintenance of structure and production of micropores. The increase of the bulk density of graphene aerogels may also be translated to the energy density of graphene supercapacitors for practical applications.

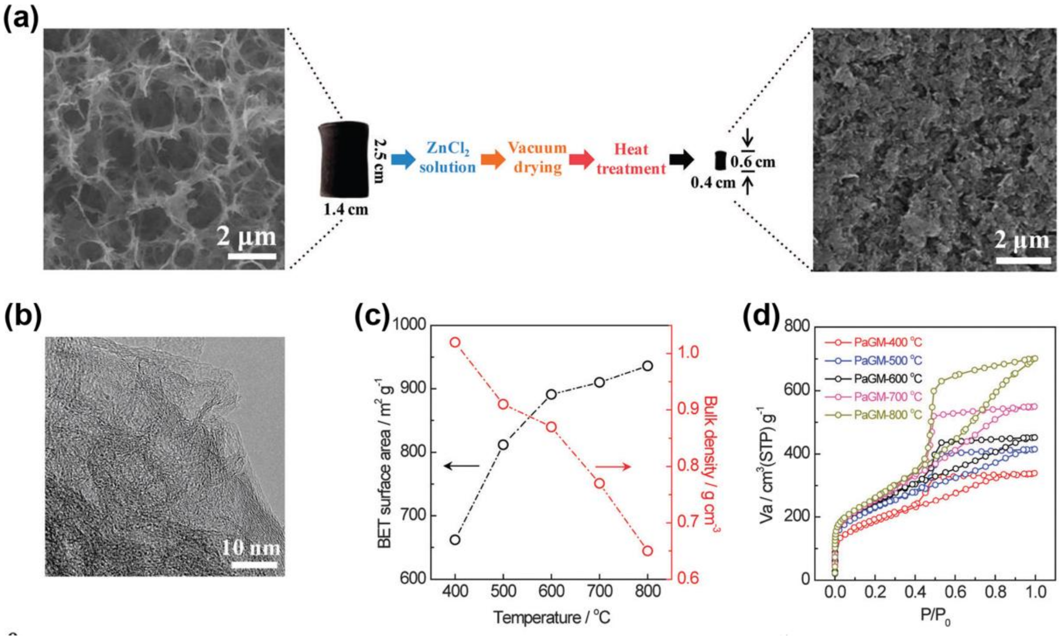

Fig. 9 Porosity tuning of graphene aerogel with $ZnCl_2$. (a) Schematic representation of the preparation process of the microporous graphene aerogel using $ZnCl_2$ as a pore-forming agent. (b) TEM image of the microporous graphene aerogel. (c) increased surface area and decreased density and (d) $N_2$ adsorption-desorption isotherms of the microporous graphene aerogel after different high temperature treatment [84].

## 3.3 Foams

Ni foams with 3D interconnected macropores are often used as current collectors to enhance electrolyte accessible surface of active materials. It was found that the stable functional graphene colloids prepared from p-phenylene diamine were positively charged in organic solutions[66]. Graphene nanosheets were loaded on the Ni foams by electrophoretic deposition and subsequent annealing in Ar (Fig. 10) [85]. The specific capacitance of the graphene on the nickel foams was 139 F·g$^{-1}$ at 3 A·g$^{-1}$ in a three-electrode cell with 6 mol·L$^{-1}$ KOH.

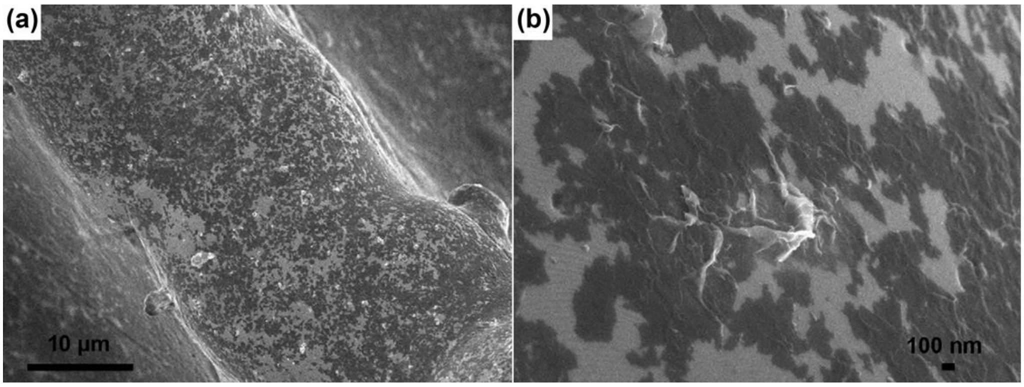

Fig. 10 SEM images of graphene nanosheets on Ni foams by electrophoretic deposition in (a) low and (b) high magnification[85].

Free-standing graphene foams were prepared using Ni foams as sacrificial templates and catalysts in a CVD process, in which the Ni foams were exposed to $CH_4$ in Ar/$H_2$ for 5 min at 1000 ºC, followed by rapid cooling [60]. The graphene foams could be immersed in the fresh mixture of the polyaniline precursors, producing graphene-polyaniline composites for supercapacitors [86].

Polyurethane (PU) sponges had a similar structure to that of the Ni foam and were used as the template to clone graphene foams. The specific capacitance of the sponge-templated graphene was 57 $F \cdot g^{-1}$ at 10 $mV \cdot s^{-1}$ in the 0.5 $mol \cdot L^{-1}$ NaCl electrolyte [87]. In order to obtain graphene foams with high specific capacitances, an activation approach was applied, in which the mixture of 1 $mg \cdot mL^{-1}$ GO and 10 $mg \cdot mL^{-1}$ KOH dissolved in a homogeneous suspension was sucked into a PU sponge and annealed at 900 °C for 2 h in an Ar flow [88]. No products were left when pure sponges were annealed in Ar, indicative of complete pyrolysis. Therefore, the only product was activated graphene which possessed micropores and mesopores besides the copied macroporous structure from the sponges. The activated sponge-templated graphene had an SSA of 2582 $m^2 \cdot g^{-1}$, which was twice of that of the activated graphene formed without using the sponge template. The increased SSA could indicate that the sponge templates prevented the aggregation of GO. A specific capacitance of 188 $F \cdot g^{-1}$ was obtained at 1 $A \cdot g^{-1}$ for the activated sponge-templated graphene in 6 $mol \cdot L^{-1}$ KOH as measured using the two-electrode cell. The sponge-templated method to prepare graphene was more facile than the Ni foam templated CVD process, which could result in higher bulk density. The activation step in the sponge-templated method prevented aggregation without compromising the desired high bulk density, promising future graphene supercapacitors of high performance.

### 3.4 Fibers

Macroscopic GO fibers were assembled by injecting GO dispersion into a coagulation bath using a syringe and rolled onto a drum. HI was used to reduce the GO fiber into graphene fiber [61]. Another work proposed a technology that a graphite tip as a positrode could withdraw graphene fibers from reduced GO nanoribbon colloids at a constant voltage [89].

The most facile method to prepare graphene fibers might be baking the GO suspension at 230 °C for 2 h, which was injected into the glass pipeline with a 0.4 mm inner diameter by a syringe. During the course of baking, graphene sheets aligned directionally to the fiber's main axis and became densely stacked, resulting in the fiber diameter reduced to 35 μm [62]. The as-prepared graphene fibers were very flexible and could be woven to various shapes and structures and embedded into the polydimethylsiloxane matrix. When inserting a stainless steel needle into a branched glass tube with a capillary tip, a hollow GO fiber could be spun in a coagulation bath (Fig. 11) [90]. An electrodeposition method was applied to grow the 3D graphene sheath on the solid graphene fiber core in the electrolyte comprising of GO aqueous suspension and $LiClO_4$. A flexible all solid state fiber supercapacitor was fabricated by intertwining the two graphene fiber core-sheath electrodes pre-coated with the $H_2SO_4$-PVA gel [91]. Its specific capacitance reached 25~40 $F\cdot g^{-1}$, while the areal capacitance and linear capacitance were 1.2~1.7 $mF\cdot cm^{-2}$ and 20 $\mu F\cdot cm^{-1}$ for a single electrode. A compressible and stretchable spring-like supercapacitor was fabricated by wrapping the wet fiber supercapacitor, whose areal and linear capacitances were close to those of the fiber core-sheath supercapacitor. Based on this method, a hollow graphene-conducting polymer fiber was fabricated by injecting a mixed solution containing GO, poly(3,4-ethylenedioxythiophene) : poly(styrenesulfonate) (PEDOT:PSS) and the reducing agent of vitamin C into a glass pipeline [92]. The hollow structure was configured by released gases during the reduction reaction of GO.

The naissance of the fiber structure enriched the macroscopic structure of graphene. Since then, 3D graphene aerogels and foams, 2D graphene films and 1D graphene fibers could have been applied in various flexible forms of supercapacitors.

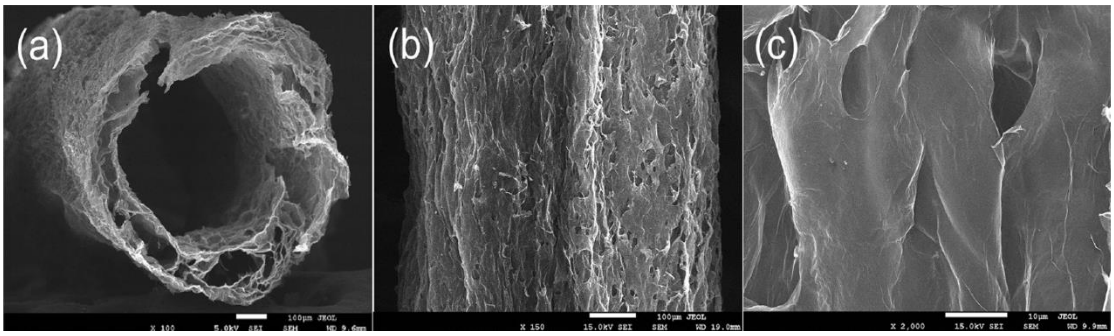

Fig. 11 SEM images of the (a) cross-section and (b, c) surface of hollow GO fiber with rapidly freeze-dried treatment [90].

The textiles, such as cotton yarns, could also be employed as the core to grow GO fibers. An electroless deposition process was exerted to produce Ni-coated cotton yarns. GO grew on the Ni-coated cotton yarns as a working electrode by electrolysis of GO in $LiClO_4$ at a constant potential in a three-electrode cell. After reduction by the hydrazine vapour, the graphene on Ni coated cotton fiber was obtained [93]. The volumetric capacitance of the composite fiber was 292.3 $F \cdot cm^{-3}$ for a single electrode at a current density of 87.9 $mA \cdot cm^{-3}$ in 1 $mol \cdot L^{-1}$ $Na_2SO_4$ as measured using a two-electrode cell. Its linear capacitance was 0.11 $F \cdot cm^{-1}$ in the PVA/LiCl gel electrolyte. Because the graphene on Ni coated cotton fiber possessed a fairly high tensile strength due to the metallic coating, it could be made into embroidery or woven into a fabric. Another example to realize the graphene fabric with giant area into clothes was to deposit graphene-polyaniline onto the polyester textile by dip-coating. The silver paste was screen printed onto one side of the textile electrode as the current collector grid, which could increase the electrical conductivity of the whole textile electrode [94]. For a 16 $cm^2$ supercapacitor textile, the areal capacitance reached 781 $mF{\cdot}cm^{-2}$ at 0.5 $mA{\cdot}cm^{-2}$, corresponding to a specific capacitance of 152 $F{\cdot}g^{-1}$ based on the total mass of graphene and polyaniline. In the absence of the current collector grid made by the silver paste, a very low areal capacitance of 0.08 $mF{\cdot}cm^{-2}$ was obtained at the same current density, indicative of the important role of the current collector grid in a textile electrode with a large area. However, the electrodeposition or immersion coating could not achieve a thick electrode on textile, let alone maintaining the porosity throughout the entire electrode thickness. To address the challenges, an alternating vacuum filtration of the dispersion of carbon nanotubes (CNTs) and graphenes through Ni-coated cotton fabric on the top of PVDF was applied [95]. A remarkable mass loading of 23.7 $mg{\cdot}cm^{-2}$ was achieved for the CNT-graphene on textile electrode. More importantly, the alternating filtration maintained nanoporous structures, resulting in the one-bilayer and ten-bilayer electrodes with similar BET values of ca. 160 $m^2{\cdot}g^{-1}$. The ultrahigh areal capacitance of 6.2 $F{\cdot}cm^{-2}$ was achieved for a single electrode at a fairly high current density of 20 $mA{\cdot}cm^{-2}$ in the 5 $mol{\cdot}L^{-1}$ LiCl aqueous electrolyte, possibly being one of the best EDLC electrodes to date. The specific capacitance of the CNT-graphene on textile electrode reached a constant value of 250 $F{\cdot}g^{-1}$ regardless of the thickness. All solid state symmetrical supercapacitor textiles in the PVA/LiCl gel electrolyte were sealed with hydrophobic polyester fabrics and treated by a water repellent spraying. The volumetric capacitance of the electrode was 107 F·cm$^{-3}$ at 20 mA·cm$^{-2}$. The feasibility to increase the area and thickness of the electrodes with proportionally enhanced performance opens an avenue toward wearable applications with high areal capacitance.

Table 2 listed the performance of graphene for aqueous supercapacitors in this section.

Table 2  Performance of graphene (G) for aqueous supercapacitors

| **Materials** [Ref.] | **SSA (m$^2$·g$^{-1}$)** | **Electrolyte** | **Capacitance (F·g$^{-1}$)** |
|---|---|---|---|
| **Molten salt G** [79] | 187 | 6 mol·L$^{-1}$ KOH | 435 (522 F·cm$^{-3}$) |
| **Holey G film** [81] | 810 | 6 mol·L$^{-1}$ KOH | 310 [a] |
| **Sponge template G** [88] | 2582 | 6 mol·L$^{-1}$ KOH | 188 [a] |
| **G-CNT textile** [95] | 160 | 5 mol·L$^{-1}$ LiCl | 250 [a] |
| | | PVA/LiCl | 107 F·cm$^{-3}$ [a] |

[a] Corresponding specific capacitance for a single electrode in the two-electrode cell, without [a] in the three-electrode cell.

## 4 Unequalisation of electrode capacitances

### 4.1 Mechanism

The main disadvantage of the aqueous supercapacitors is that their specific energy is not as high as those in organic electrolytes, including ionic liquid, let alone lithium ion batteries. This is understandable because, according to Equation (1), the cell voltage is more decisive than specific capacitance of the electrode materials for the specific energy. The theoretical voltage for water decomposition into hydrogen and oxygen gases is 1.23 V, which would limit the specific energy of aqueous supercapacitors. Fortunately, the gas evolution reactions in the electrolyte are also affected by the interaction of the electrode materials with the electrolyte, which may be affected by pH. It was demonstrated that a neutral electrolyte, KCl, had a potential window of 2.00 V which is wider than those of acidic and alkaline electrolytes [96]. Nevertheless, the cell voltage of the symmetrical AC supercapacitor in a neutral electrolyte of $Li_2SO_4$ could not be higher than 1.60 V to ensure a stable performance [97].

Because the nascent hydrogen produced from water decomposition is immediately absorbed in the micropores of AC, an overpotential for $H_2$ molecule formation and gas evolution is needed. The theoretical potential for $H_2$ evolution on the AC electrode was calculated to be −0.38 V vs. the normal hydrogen electrode (NHE) at pH value of 6.4. For the $MnO_2$ electrode, positive scanning of the polarization potential is expected to invoke either the reactions of Mn(IV) to Mn(VII) or $O_2$ evolution from water decomposition. In a neutral or low pH electrolyte, $O_2$ evolution may occur at a potential more positive than the thermodynamic equilibrium potential, largely because $H^+$ could be generated on the $MnO_2$ electrode under positive polarization, making it difficult for $H_2O$ oxidation to produce the $O_2$ gas. The positive polarization potential achieved a maximum at pH of 6.4, resulting in an extension of the cell voltage to 2.00 V for an asymmetrical supercapacitor in a neutral electrolyte assembled from a $MnO_2$ positrode and an AC negatrode [98].

The amount of charge, Q, stored in each of the positrode and negatrode must be the same, which is governed by Equation (4),

$$Q = C_p U_p = C_n U_n = C_{pm} m_p U_p = C_{nm} m_n U_n \qquad (4)$$

where $C_p$ and $C_n$, $C_{pm}$ and $C_{nm}$, and $U_p$ and $U_n$ are the capacitances, specific capacitances, and potential ranges of the positrode and negatrode, respectively. Conventionally, in the symmetrical supercapacitors, capacitance equalization of the two electrodes is a necessity to maximize specific energy because the positrode and negatrode have the same working potential range. Generally, the exploitable potential range of a positrode, $U^o_p$, is narrower than that of the negatrode, $U^o_n$, in many asymmetrical cells with an AC negatrode, e.g. (–) AC | neutral aqueous electrolyte | $MnO_2$ (+). When the positrode and negatrode in an asymmetrical supercapacitor are equalized in capacitance like in the symmetrical one, the cell voltage will be limited by the positrode with a smaller exploitable potential range. Ideally, the cell voltage should cover the whole exploitable potential ranges of positrode and negatrode. As $C_{pm}$ and $C_{nm}$ are determined by the nature of the electrode materials, the mass ratio $m_p/m_n$ is related to the potential ranges of the positrode and negatrode. Although $U_n$ and $U_p$ are next to each other, $U^o_p$ and $U^o_n$ may be often overlapping partially. It was found that the cell voltage and $U_n$ increased with increasing $C_p/C_n$ in the asymmetrical supercapacitors assembled by electrodeposited polyaniline (–) and AC (+) in an acidic electrolyte (Fig. 12a) [99]. More importantly, the equi-potential, or the potential of zero voltage, $E_{0V}$, i.e. the potential at the fully discharged state, moved towards more negative values, which was deduced by a small charging peak on the CVs of the asymmetrical cell corresponding to the constant potential of 0.78 V vs. Ag/AgCl for the polyaniline electrode as well as Equation (4). It meant that $U_p$ also slightly increased. The specific energy had the same increasing trend as the cell voltage. Hence, the mass ratio $m_p/m_n$ is tightly associated with the potential of zero voltage [100]. In fact, $E_{0V}$ in the experiments was not consistent with the estimation, for instance, the potential of Mn(IV) to Mn(II) reduction for the (−) AC | neutral aqueous electrolyte | $MnO_2$ (+) asymmetrical supercapacitors. Increasing the mass ratio, i.e. $C_p/C_n$, was tried to extend the $U_n$ and the voltage of the (–) AC | neutral aqueous electrolyte | $MnO_2$ (+) cell [101]. Monitoring the cycle life is the more convincing and reliable way for validating a cell, rather than the coulombic efficiency in the initial charge-discharge cycles.

Conventionally, asymmetrical supercapacitors were assembled by different materials with different exploitable potential ranges to gain a higher cell voltage than the symmetrical ones. However, the asymmetrical concept could extend to the same material with different masses if the material behaves differently in different exploitable potential ranges. A commercial Cabot Monarch® 1300 pigment black (CMPB) exhibited a very wide potential window in neutral electrolytes when measured in a three-electrode cell, reaching close to 2.20 V in $K_2SO_4$. However, $E_{0V}$ is closer to the positive potential limit of the CMPB electrode, so that the symmetrical supercapacitor had only a 1.60 V cell voltage. Unequalization of electrode capacitances was achieved by using the same CMPB material of different masses (hence different capacitances) to make the positrode and negatrode, hence the actually exploited potential ranges of the two electrodes, $U_n$ and $U_p$, were adjusted, leading to a sufficiently high maximum cell voltage of 1.90 V with a stable cyclic performance (Fig. 12b) [102]. When the asymmetrical cell was charged to 1.9 V, the initial positive potential limit was as high as 1.05 V vs. Ag/AgCl, but dropped to and stabilized at about 0.86 V after 800 cycles until the end of cycling test (6000 cycles). In a separate test in the three electrode cell, the positive potential limit was found to be 0.90 V. Thus, this final stable potential of the positrode at 0.86 V in the cycling test is the evidence that anodic oxidation of the CMPB electrode should have been responsible for performance decay when the cycling test was carried out at cell voltages higher than 1.90 V. However, it was also noticed that the stable negatrode potential recorded in the cycling test was still about –1.00 V, far more positive than the negative potential limit of –1.4 V for the CMPB electrode. This is indication that there is still room to further increase the cell voltage, calling for more investigation.

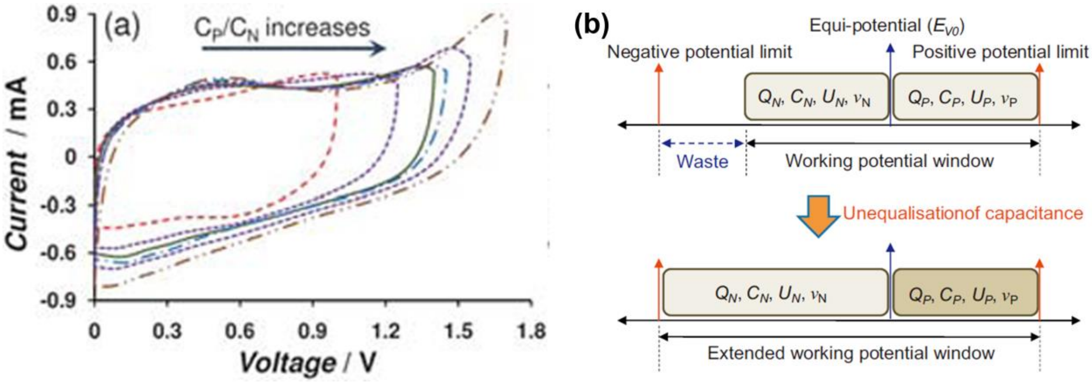

Fig. 12 (a) CVs of asymmetrical supercapacitors with CMPB negatrode and a PAN–CNT positrode at various $C_p/C_n$ ratios with the charging current peak at the same scan rate [99]. (b) A strategy to increase the operating voltage of supercapacitors with the same material for both the positrode and negatrode via unequalisation of electrode capacitances [102].

The specific energy, $E_{\mathrm{sp}}$, of a supercapacitor (cell) is calculated by Equation (5) below.

$$E_{sp} = \frac{C_{cell}U^2}{2(m_{+} + m_{-})} \tag{5}$$

where $C_{\mathrm{cell}}$ and $U$ are the capacitance and maximum cell voltage of the supercapacitor, and $m_+$ and $m_-$ are the masses of the positrode and negatrode, respectively. Interestingly, if $C_{\mathrm{cell}}$, $U$ and the sum of $(m_+ + m_-)$ are all fixed constants, Equation (5) predicts a maximum $E_{\mathrm{sp}}$ when $m_+ = m_-$. This is obviously not the case in the above discussion in relation with Equation (4) which allows changes in both $C_{\mathrm{cell}}$ and $U$. Further, what is not mentioned in both Equations (4) and (5) is the importance of the equi-potential of zero voltage, $E_{0\mathrm{V}}$, which is a key parameter to determine both $U_{\mathrm{n}}$ and $U_{\mathrm{p}}$. It is worth noting that in conjunction with equi-mass principle of Equation (5), the equi-potential of graphitic materials, typically graphene, could be adjusted in an organic 1 mol·L$^{-1}$ $LiPF_6$ electrolyte. After electrochemical charge injection, the original $E_{0V}$ of 3.50 V of graphene was adjusted to 1.16 V vs. Li/Li$^+$, resulting in a cell voltage increase from 3.00 to 4.30 V [103].

### 4.2 Asymmetrical supercapacitors

A classic example of asymmetrical supercapacitors is that assembled with a $MnO_2$ positrode and an AC negatrode in a neutral aqueous electrolyte. The (–) AC | $KNO_3$ | $MnO_2$ (+) supercapacitor was found to a maximum specific energy of 21 Wh·kg$^{-1}$ when the cell voltage reached an optimal 2.00 V when the pH was 6.84 for the electrolyte [98].

Instead of AC, graphene was used to make the negative electrode in the asymmetrical supercapacitor. The $MnO_2$ nanowires were loaded on graphene as the positrode material in order to increase the electric conductivity. The (–) graphene | 1 $mol·L^{-1}$ $Na_2SO_4$ | $MnO_2$-graphene (+) asymmetrical supercapacitor had a specific energy of 30 $Wh·kg^{-1}$ at a small specific current (0.1 $A·g^{-1}$) [104]. Then, a microwave treatment was applied to irradiate the $KMnO_4$ in graphene suspension, leading to a high specific capacitance of 310 $F·g^{-1}$ at 2 $mV·s^{-1}$ for the synthetic $MnO_2$-graphene composite. Therefore, the (–) AC | $Na_2SO_4$ | $MnO_2$-graphene (+) cell reached a specific energy of 51 $Wh·kg^{-1}$ at 2 $mV·s^{-1}$ while the cell voltage was 1.80 V [105]. Although $Mn_3O_4$ had lower specific capacitance than $MnO_2$ [106], it seemed that the birnessite $Na_{0.5}MnO_2$ nanosheets prepared by electrochemical oxidation of $Mn_3O_4$ via cyclic voltammetry (CV) in the $Na_2SO_4$ electrolyte were attractive because of an extended exploitable potential range [107]. The specific capacitance was 311 $F·g^{-1}$ at 1 $A·g^{-1}$. When $Na_{0.5}MnO_2$ was combined with $Fe_3O_4$–C [107] or AC [108], the cell voltages reached 2.60 and 2.70 V while the specific energies were 81 and 61 $Wh·kg^{-1}$, respectively. It was also found that the $Ni_{0.25}Mn_{0.75}O$ arrays with AC could achieve a cell voltage of 2.40 V when a new phase transformation occurred to the poorly crystallized $LiNi_{0.5}Mn_{1.5}O_4$ electrode after CV activation in the LiCl aqueous electrolyte [109].

Some other commonly claimed asymmetrical supercapacitors include (–) AC | acidic aqueous electrolyte | conductive polymer (+) and (–) AC | alkaline aqueous electrolyte | Ni–Co oxide (+). The former is a good example of the combination of an EDL capacitive negatrode with a pseudocapacitive positrode. The latter, however, comprises a positrode made from $NiCo_2O_4$ [110-112], $Co(OH)_2$ [113], $Ni(OH)_2$ [114], and Ni–Co layered double hydroxide [115]. Whilst these electrochemical cells should be capable of charge storage, they are not truly supercapacitors because the Ni-Co oxides or hydroxides behave more like a battery electrode material. These hybrid electrochemical cells are now defined as supercapattery which is beyond the scope of this review.

## 5 Conclusions and outlook

In conclusion, activated carbons (ACs) are generally good materials for making either the positrode or negatrode or both in supercapacitors. They can be prepared by the conventional two-step method, including carbonization and activation at high temperatures. The precursors for making ACs, including those with special shapes similar to that of carbon nanotubes and graphene, have been shown to be crucial in affecting the properties of the produced ACs. Although the extra post vacuum annealing can improve the electrical and electrochemical properties, the molecular level one-step activation method can be a better choice for production of ACs from some biomass precursors of low structural orders with a low cost and high performance. Graphitization of AC can be fulfilled by $FeCl_3$ catalysis during the activation, which increases the electrical conductivity. Hetero-atom doping is also an efficient means to add pseudocapacitance into the carbon materials. Template method can produce the hierarchical porous structures in carbon materials which facilitate the electrolyte transfer. Metal-organic frameworks used as a self-template and a new carbon precursor can give rise to tailored porous carbon or graphene, which have novel academic values.

Graphene can also be the excellent electrode materials for supercapacitors due to large theoretic specific surface area and the partial electron delocalisation by residual O atoms according to the recent developed theory. Various structures of graphene can be made as electrode materials for supercapacitors, including graphene powders, graphene films, graphene aerogels, graphene foams and graphene fibers. Activation can also produce micropores in graphene, which is like those in AC. Self-propagating high temperature synthesis can produce mesoporous graphene powders by the magnesiothermic reaction, while molten salt technology mesoporous graphene with a high packing density. Macroporous graphene hydrogel can be produced by hydrothermal treatment of graphite oxide suspension. The graphene hydrogel can also be transferred into the film structure. Hierarchical porosity can be yielded by $H_2O_2$ etching or $ZnCl_2$ activation of the macroporous graphene hydrogel. Activated graphene foams can be prepared by sucking the mixture of GO and KOH using sponges as templates, which can exert high performance in supercapacitors. Graphene fibers prepared by the cast-like method can be used a core to grow graphene by electrodeposition. Additionally, graphene based materials can grow on the textile by electrodeposition, dip-coating or filtration, which can be weaved into clothes with large area or thick loading. These graphene based fibers and textiles have a promise application in flexible and wearable supercapacitors.

Besides the desirable specific capacitance arising from the optimal AC and graphene electrodes, the cell voltage is paramount to increase the specific energy for supercapacitors. Extension of cell voltage is rationally fulfilled by asymmetrical supercapacitors, in which the balance of the charge in the positrode and negatrode must be complied with. Increase of $C_p/C_n$ can thoroughly utilize the whole exploitable potential ranges of the positrode and negatrode in the aqueous asymmetrical supercapacitors.

High energy consumption during calcination, low packing density and yield of carbon are the main bottleneck in fabrication of ACs for industrial application. Recently, carbon spheres were loaded within the macropores in rice straw-derived carbon [116]. Therefore, filling nano-micro carbon into the macropores in bulk ACs is also a facile method to increase packing density of carbon. As we know, activation is a carbon removal process which produces $CO_2$ gas and leave behind micropores in bulk carbon. When carboxymethylcellulose sodium, a binder with high O content, was used as a precursor, too little product is to be collected. It is reported that Mg powders could lead to a carbon regeneration process when reacting with released $CO_2$ during activation of carboxymethylcellulose sodium [117]. Although metal Mg is very expensive, the carbon regeneration process to balance the carbon removal process during activation is a new thought to improve carbon yield.

Two new trends in the development of aqueous supercapacitors have emerged. Firstly, when the redox active hydroquinone was added into the electrolyte (which is then referred as a redox electrolyte) of a carbon based supercapacitor, a large increase to 900 $F \cdot g^{-1}$ in specific capacitance was claimed [118]. Similarly, addition of the redox active salt of $K_3Fe(CN)_6$ in the aqueous electrolyte could lead to confinement of the salt or its ions in a solid-like state within the electrode, and hence the counter ion effect to increase the specific capacitance of the carbon electrode [119,120]. Whilst recognizing the contribution to charge storage capacity, it has been pointed out that the increased charge storage capacity from the redox electrolyte is actually Nernstian (i.e. battery-like). Therefore, the device is no longer a supercapacitor, and hence its storage performance should not be analyzed in terms of capacitance [121]. The term supercapattery is more appropriate for description of such hybrid devices in which charge storage is achieved in both the capacitive and Nernstian mechanisms [1, 122]. The other trend of development is the application of the 3D printing technology in fabrication of micro-supercapacitors, which requires the ink of the electrode materials with appropriate viscosity as well as shear-thinning rheological properties [123].

The innovation in the production of AC and graphene may bring out the prospect toward supercapacitors with high performance and low cost. The incorporation of the redox components and the 3D printing technology are two of the new trends to develop aqueous supercapacitors. With the unremitting efforts from multidiscipline, it is believed that the AC and graphene materials from new precursors and production methods can open up a significant vista for aqueous supercapacitors in the near future.

## References

(1) Chen, G. Z. *Int. Mater. Rev.* **2017**, *62*, 173. doi: 10.1080/09506608.2016.1240914

(2) Zhang, X.; Zhang, H.; Li, C.; Wang, K.; Sun, X.; Ma, Y. *RSC Adv.* **2014**, *4*, 45862. doi: 10.1039/c4ra07869a

(3) Chen, Y.; Chen, G. Z. Building porous graphene architectures for

electrochemical energy storage devices. In Innovations in engineered porous materials for energy generation and storage applications; Rajagopalan, R.; Balakrishnan, A. Eds.; CRC press: Boca Raton, 2018; pp 86−108.

(4) Inagaki, M.; Konno, H.; Tanaike, O. *J. Power Sources* **2010**, *195*, 7880. doi: 10.1016/j.jpowsour.2010.06.036

(5) Hibino, T.; Kobayashi, K.; Nagao, M.; Kawasaki, S. *Sci. Rep.* **2015**, *5*, 7903. doi: 10.1038/srep07903

(6) Sevilla, M.; Mokaya, R. *Energy Environ. Sci.* **2014**, *7*, 1250. doi: 10.1039/c3ee43525c

(7) Harris, P. J. F.; Liu, Z.; Suenaga, K. *J. Phys.: Condens. Matter* **2008**, *20*, 362201. doi: 10.1088/0953-8984/20/36/362201

(8) Peigney, A.; Laurent, C.; Flahaut, E.; Bacsa, R. R.; Rousset, A. *Carbon* **2001**, *39*, 507. doi: 10.1016/s0008-6223(00)00155-x

(9) Zhang, Y.; Tan, Y.-W.; Stormer, H. L.; Kim, P. *Nature* **2005**, *438*, 201. doi: 10.1038/nature04235

(10) Liu, F.; Ming, P.; Li, J. *Phys. Rev. B* **2007**, *76*, 064120. doi: 10.1103/PhysRevB.76.064120

(11) Stankovich, S.; Dikin, D. A.; Piner, R. D.; Kohlhaas, K. A.; Kleinhammes, A.; Jia, Y.; Wu, Y.; Nguyen, S. T.; Ruoff, R. S. *Carbon* **2007**, *45*, 1558. doi: 10.1016/j.carbon.2007.02.034

(12) Stoller, M. D.; Park, S.; Zhu, Y.; An, J.; Ruoff, R. S. *Nano Lett.* **2008**, *8*, 3498. doi: 10.1021/nl802558y

(13) Li, D.; Muller, M. B.; Gilje, S.; Kaner, R. B.; Wallace, G. G. *Nat. Nanotechnol.* **2008**, *3*, 101. doi: 10.1038/nnano.2007.451

(14) Li, J.; O'Shea, J.; Hou, X.; Chen, G. Z. *Chem. Commun.* **2017**, *53*, 10414. doi: 10.1039/c7cc04344a

(15) Rouquerol, J.; Avnir, D.; Fairbridge, C. W.; Everett, D. H.; Haynes, J. H.; Pernicone, N.; Ramsay, J. D. F.; Sing, K. S. W.; Unger, K. K. *Pure Appl. Chem.* **1994**, *66*, 1739. doi: 10.1351/pac199466081739

(16) Ibarra, J.; Moliner, R.; Palacios, J. *Fuel* **1991**, *70*, 727. doi: 10.1016/0016-2361(91)90069-M

(17) Ahmadpour, A.; Do, D. D. *Carbon* **1996**, *34*, 471. doi: 10.1016/0008-6223(95)00204-9

(18) Hayashi, J. i.; Kazehaya, A.; Muroyama, K.; Watkinson, A. P. *Carbon* **2000**, *38*, 1873. doi: 10.1016/S0008-6223(00)00027-0

(19) Saha, D.; Li, Y.; Bi, Z.; Chen, J.; Keum, J. K.; Hensley, D. K.; Grappe, H. A.; Meyer, H. M.; Dai, S.; Paranthaman, M. P.; Naskar, A. K. *Langmuir* **2014**, *30*, 900. doi: 10.1021/la404112m

(20) Hao, P.; Zhao, Z.; Tian, J.; Li, H.; Sang, Y.; Yu, G.; Cai, H.; Liu, H.; Wong, C. P.; Umar, A. *Nanoscale* **2014**, *6*, 12120. doi: 10.1039/c4nr03574g

(21) Su, X.-L.; Chen, J.-R.; Zheng, G.-P.; Yang, J.-H.; Guan, X.-X.; Liu, P.; Zheng, X.-C. *Appl. Surf. Sci.* **2018**, *436*, 327. doi: 10.1016/j.apsusc.2017.11.249

(22) Xie, L.; Sun, G.; Su, F.; Guo, X.; Kong, Q.; Li, X.; Huang, X.; Wan, L.; song, W.; Li, K.; Lv, C.; Chen, C.-M. *J. Mater. Chem. A* **2016**, *4*, 1637. doi:

10.1039/c5ta09043a

(23) Li, Y.; Wang, G.; Wei, T.; Fan, Z.; Yan, P. *Nano Energy* **2016**, *19*, 165. doi: 10.1016/j.nanoen.2015.10.038

(24) Wang, H.; Xu, Z.; Li, Z.; Cui, K.; Ding, J.; Kohandehghan, A.; Tan, X.; Zahiri, B.; Olsen, B. C.; Holt, C. M. B.; Mitlin, D. *Nano Lett.* **2014**, *14*, 1987. doi: 10.1021/nl500011d

(25) Tian, W.; Gao, Q.; Tan, Y.; Yang, K.; Zhu, L.; Yang, C.; Zhang, H. *J. Mater. Chem. A* **2015**, *3*, 5656. doi: 10.1039/c4ta06620k

(26) Li, D.; Zhang, J.; Wang, Z.; Jin, X. *Acta Phys.-Chim. Sin.* **2017**, *33*, 2245. [李道琰，张基琛，王志勇，金先波．物理化学学报，**2017**, 33, 2245.] doi: 10.3866/pku.whxb201705241

(27) Zhang, L.; Gu, H.; Sun, H.; Cao, F.; Chen, Y.; Chen, G. Z. *Carbon* **2018**, *132*, 573. doi: 10.1016/j.carbon.2018.02.100

(28) Mao, N.; Wang, H.; Sui, Y.; Cui, Y.; Pokrzywinski, J.; Shi, J.; Liu, W.; Chen, S.; Wang, X.; Mitlin, D. *Nano Research* **2017**, *10*, 1767. doi: 10.1007/s12274-017-1486-6

(29) Yan, J.; Wei, T.; Qiao, W.; Fan, Z.; Zhang, L.; Li, T.; Zhao, Q. *Electrochem. Commun.* **2010**, *12*, 1279. doi: DOI: 10.1016/j.elecom.2010.06.037

(30) Zhang, H.; Zhang, X.; Ma, Y. *Electrochim. Acta* **2015**, *184*, 347. doi: 10.1016/j.electacta.2015.10.089

(31) Su, H.; Zhang, H.; Liu, F.; Chun, F.; Zhang, B.; Chu, X.; Huang, H.; Deng, W.; Gu, B.; Zhang, H.; Zheng, X.; Zhu, M.; Yang, W. *Chem. Eng. J.* **2017**, *322*, 73.

doi: 10.1016/j.cej.2017.04.012

(32) Tang, K.; Chang, J.; Cao, H.; Su, C.; Li, Y.; Zhang, Z.; Zhang, Y. *ACS Sustainable Chemistry & Engineering* **2017**, *5*, 11324. doi: 10.1021/acssuschemeng.7b02307

(33) Feng, L.; Wang, K.; Zhang, X.; Sun, X.; Li, C.; Ge, X.; Ma, Y. *Adv. Funct. Mater.* **2018**, *28*, 1704463. doi: 10.1002/adfm.201704463

(34) Alabadi, A.; Yang, X.; Dong, Z.; Li, Z.; Tan, B. *J. Mater. Chem. A* **2014**, *2*, 11697. doi: 10.1039/c4ta01215a

(35) Kim, M.; Puthiaraj, P.; Qian, Y.; Kim, Y.; Jang, S.; Hwang, S.; Na, E.; Ahn, W.-S.; Shim, S. E. *Electrochim. Acta* **2018**, *284*, 98. doi: 10.1016/j.electacta.2018.07.096

(36) Wei, X.; Wan, S.; Jiang, X.; Wang, Z.; Gao, S. *ACS Appl. Mater. Interfaces* **2015**, *7*, 22238. doi: 10.1021/acsami.5b05022

(37) Sun, L.; Tian, C.; Li, M.; Meng, X.; Wang, L.; Wang, R.; Yin, J.; Fu, H. *J. Mater. Chem. A* **2013**, *1*, 6462. doi: 10.1039/c3ta10897j

(38) Graf, D.; Molitor, F.; Ensslin, K.; Stampfer, C.; Jungen, A.; Hierold, C.; Wirtz, L. *Nano Lett.* **2007**, *7*, 238. doi: 10.1021/nl061702a

(39) Tian, W.; Gao, Q.; Tan, Y.; Li, Z. *Carbon* **2017**, *119*, 287. doi: 10.1016/j.carbon.2017.04.050

(40) Li, B.; Dai, F.; Xiao, Q.; Yang, L.; Shen, J.; Zhang, C.; Cai, M. *Energy Environ. Sci.* **2016**, *9*, 102. doi: 10.1039/c5ee03149d

(41) Ma, C.; Chen, X.; Long, D.; Wang, J.; Qiao, W.; Ling, L. *Carbon* **2017**, *118*,

699. doi: 10.1016/j.carbon.2017.03.075

(42) Song, Z.; Zhu, D.; Li, L.; Chen, T.; Duan, H.; Wang, Z.; Lv, Y.; Xiong, W.; Liu, M.; Gan, L. *J. Mater. Chem. A* **2019**, *7*, 1177. doi: 10.1039/c8ta10158b

(43) Li, Z.; Xu, Z.; Wang, H.; Ding, J.; Zahiri, B.; Holt, C. M. B.; Tan, X.; Mitlin, D. *Energy Environ. Sci.* **2014**, *7*, 1708. doi: 10.1039/C3EE43979H

(44) Xia, X.; Zhang, Y.; Fan, Z.; Chao, D.; Xiong, Q.; Tu, J.; Zhang, H.; Fan, H. J. *Adv. Energy Mater.* **2015**, *5*, 1401709. doi: 10.1002/aenm.201401709

(45) Wang, Q.; Yan, J.; Wang, Y.; Wei, T.; Zhang, M.; Jing, X.; Fan, Z. *Carbon* **2014**, *67*, 119. doi: 10.1016/j.carbon.2013.09.070

(46) Li, C.; Zhang, X.; Wang, K.; Sun, X.; Ma, Y. *J. Power Sources* **2018**, *400*, 468. doi: 10.1016/j.jpowsour.2018.08.013

(47) Li, C.; Zhang, X.; Wang, K.; Sun, X.; Ma, Y. *Carbon* **2018**, *140*, 237. doi: 10.1016/j.carbon.2018.08.044

(48) Ning, G.; Fan, Z.; Wang, G.; Gao, J.; Qian, W.; Wei, F. *Chem. Commun.* **2011**, *47*, 5976. doi: 10.1039/c1cc11159k

(49) Fan, Z.; Liu, Y.; Yan, J.; Ning, G.; Wang, Q.; Wei, T.; Zhi, L.; Wei, F. *Adv. Energy Mater.* **2012**, *2*, 419. doi: 10.1002/aenm.201100654

(50) Liu, B.; Shioyama, H.; Akita, T.; Xu, Q. *J. Am. Chem. Soc.* **2008**, *130*, 5390. doi: 10.1021/ja7106146

(51) Jiang, H.-L.; Liu, B.; Lan, Y.-Q.; Kuratani, K.; Akita, T.; Shioyama, H.; Zong, F.; Xu, Q. *J. Am. Chem. Soc.* **2011**, *133*, 11854. doi: 10.1021/ja203184k

(52) Chaikittisilp, W.; Hu, M.; Wang, H.; Huang, H.-S.; Fujita, T.; Wu, K. C. W.;

Chen, L.-C.; Yamauchi, Y.; Ariga, K. *Chem. Commun.* **2012**, *48*, 7259. doi: 10.1039/c2cc33433j

(53) Amali, A. J.; Sun, J.-K.; Xu, Q. *Chem. Commun.* **2014**, *50*, 1519. doi: 10.1039/c3cc48112c

(54) Sun, H.; Gu, H.; Zhang, L.; Chen, Y. *Mater. Lett.* **2018**, *216*, 123. doi: 10.1016/j.matlet.2018.01.009

(55) Salunkhe, R. R.; Young, C.; Tang, J.; Takei, T.; Ide, Y.; Kobayashi, N.; Yamauchi, Y. *Chem. Commun.* **2016**, *52*, 4764. doi: 10.1039/c6cc00413j

(56) Pachfule, P.; Shinde, D.; Majumder, M.; Xu, Q. *Nat. Chem.* **2016**, *8*, 718. doi: 10.1038/nchem.2515

(57) Kosynkin, D. V.; Higginbotham, A. L.; Sinitskii, A.; Lomeda, J. R.; Dimiev, A.; Price, B. K.; Tour, J. M. *Nature* **2009**, *458*, 872. doi: 10.1038/nature07872

(58) Yang, X.; Cheng, C.; Wang, Y.; Qiu, L.; Li, D. *Science* **2013**, *341*, 534. doi: 10.1126/science.1239089

(59) Xu, Y.; Sheng, K.; Li, C.; Shi, G. *ACS Nano* **2010**, *4*, 4324. doi: 10.1021/nn101187z

(60) Chen, Z.; Ren, W.; Gao, L.; Liu, B.; Pei, S.; Cheng, H.-M. *Nat. Mater.* **2011**, *10*, 424. doi: 10.1038/nmat3001

(61) Xu, Z.; Gao, C. *Nat. Commun.* **2011**, *2*, 571. doi: 10.1038/ncomms1583

(62) Dong, Z.; Jiang, C.; Cheng, H.; Zhao, Y.; Shi, G.; Jiang, L.; Qu, L. *Adv. Mater.* **2012**, *24*, 1856. doi: 10.1002/adma.201200170

(63) Shin, H.-J.; Kim, K. K.; Benayad, A.; Yoon, S.-M.; Park, H. K.; Jung, I.-S.; Jin,

M. H.; Jeong, H.-K.; Kim, J. M.; Choi, J.-Y.; Lee, Y. H. *Adv. Funct. Mater.* **2009**, *19*, 1987. doi: 10.1002/adfm.200900167

(64) Fan, X.; Peng, W.; Li, Y.; Li, X.; Wang, S.; Zhang, G.; Zhang, F. *Adv. Mater.* **2008**, *20*, 4490. doi: 10.1002/adma.200801306

(65) Wang, G.; Yang, J.; Park, J.; Gou, X.; Wang, B.; Liu, H.; Yao, J. *J. Phys. Chem. C* **2008**, *112*, 8192. doi: 10.1021/jp710931h

(66) Chen, Y.; Zhang, X.; Yu, P.; Ma, Y. *Chem. Commun.* **2009**, 4527. doi: 10.1039/B907723E

(67) Zhang, J.; Yang, H.; Shen, G.; Cheng, P.; Zhang, J.; Guo, S. *Chem. Commun.* **2010**, *46*, 1112. doi: 10.1039/B917705A

(68) Chen, Y.; Zhang, X.; Zhang, D.; Yu, P.; Ma, Y. *Carbon* **2011**, *49*, 573. doi: 10.1016/j.carbon.2010.09.060

(69) Pei, S.; Zhao, J.; Du, J.; Ren, W.; Cheng, H.-M. *Carbon* **2010**, *48*, 4466. doi: 10.1016/j.carbon.2010.08.006

(70) Schniepp, H. C.; Li, J.-L.; McAllister, M. J.; Sai, H.; Herrera-Alonso, M.; Adamson, D. H.; Prud'homme, R. K.; Car, R.; Saville, D. A.; Aksay, I. A. *J. Phys. Chem. B* **2006**, *110*, 8535. doi: 10.1021/jp060936f

(71) Yan, J.; Wang, Q.; Wei, T.; Jiang, L.; Zhang, M.; Jing, X.; Fan, Z. *ACS Nano* **2014**, *8*, 4720. doi: 10.1021/nn500497k

(72) Zhu, Y.; Murali, S.; Stoller, M. D.; Ganesh, K. J.; Cai, W.; Ferreira, P. J.; Pirkle, A.; Wallace, R. M.; Cychosz, K. A.; Thommes, M.; Su, D.; Stach, E. A.; Ruoff, R. S. *Science* **2011**, *332*, 1537. doi: 10.1126/science.1200770

(73) Chen, Y.; Zhang, X.; Zhang, H.; Sun, X.; Zhang, D.; Ma, Y. *RSC Advances* **2012**, *2*, 7747. doi: 10.1039/C2RA20667F

(74) Kim, H. K.; Bak, S. M.; Lee, S. W.; Kim, M. S.; Park, B.; Lee, S. C.; Choi, Y. J.; Jun, S. C.; Han, J. T.; Nam, K. W.; Chung, K. Y.; Wang, J.; Zhou, J.; Yang, X. Q.; Roh, K. C.; Kim, K. B. *Energy Environ. Sci.* **2016**, *9*, 1270. doi: 10.1039/c5ee03580e

(75) Li, C.; Zhang, X.; Wang, K.; Sun, X.; Liu, G.; Li, J.; Tian, H.; Li, J.; Ma, Y. *Adv. Mater.* **2017**, *29*, 1604690. doi: 10.1002/adma.201604690

(76) Chakrabarti, A.; Lu, J.; Skrabutenas, J. C.; Xu, T.; Xiao, Z.; Maguire, J. A.; Hosmane, N. S. *J. Mater. Chem.* **2011**, *21*, 9491. doi: 10.1039/c1jm11227a

(77) Zhang, H.; Zhang, X.; Sun, X.; Zhang, D.; Lin, H.; Wang, C.; Wang, H.; Ma, Y. *ChemSusChem* **2013**, *6*, 1084. doi: 10.1002/cssc.201200904

(78) Strauss, V.; Marsh, K.; Kowal, M. D.; El-Kady, M.; Kaner, R. B. *Adv. Mater.* **2018**, *30*, 1704449. doi: 10.1002/adma.201704449

(79) Lin, S.; Zhang, C.; Wang, Z.; Dai, S.; Jin, X. *Adv. Energy Mater.* **2017**, *7*, 1700766. doi: 10.1002/aenm.201700766

(80) Liu, Y.; Cai, X.; Luo, B.; Yan, M.; Jiang, J.; Shi, W. *Carbon* **2016**, *107*, 426. doi: 10.1016/j.carbon.2016.06.025

(81) Xu, Y.; Lin, Z.; Zhong, X.; Huang, X.; Weiss, N. O.; Huang, Y.; Duan, X. *Nat. Commun.* **2014**, *5*, 4554. doi: 10.1038/ncomms5554

(82) Bai, H.; Li, C.; Wang, X.; Shi, G. *J. Phys. Chem. C* **2011**, *115*, 5545. doi: 10.1021/jp1120299

(83) Xiong, Z.; Liao, C.; Han, W.; Wang, X. *Adv. Mater.* **2015**, *27*, 4469. doi: 10.1002/adma.201501983

(84) Li, H.; Tao, Y.; Zheng, X.; Luo, J.; Kang, F.; Cheng, H.-M.; Yang, Q.-H. *Energy Environ. Sci.* **2016**, *9*, 3135. doi: 10.1039/c6ee00941g

(85) Chen, Y.; Zhang, X.; Yu, P.; Ma, Y. *J. Power Sources* **2010**, *195*, 3031. doi: 10.1016/j.jpowsour.2009.11.057

(86) Kulkarni, S. B.; Patil, U. M.; Shackery, I.; Sohn, J. S.; Lee, S.; Park, B.; Jun, S. *J. Mater. Chem. A* **2014**, *2*, 4989. doi: 10.1039/c3ta14959e

(87) Yang, Z.-Y.; Jin, L.-J.; Lu, G.-Q.; Xiao, Q.-Q.; Zhang, Y.-X.; Jing, L.; Zhang, X.-X.; Yan, Y.-M.; Sun, K.-N. *Adv. Funct. Mater.* **2014**, *24*, 3917. doi: 10.1002/adfm.201304091

(88) Xu, J.; Tan, Z.; Zeng, W.; Chen, G.; Wu, S.; Zhao, Y.; Ni, K.; Tao, Z.; Ikram, M.; Ji, H.; Zhu, Y. *Adv. Mater.* **2016**, *28*, 5222. doi: 10.1002/adma.201600586

(89) Jang, E. Y.; Carretero-González, J.; Choi, A.; Kim, W. J.; Kozlov, M., E. ; Kim, T.; Kang, T. J.; Baek, S. J.; Kim, D. W.; Park, Y. W.; Baughman, R. H.; Kim, Y. H. *Nanotechnology* **2012**, *23*, 235601. doi: 10.1088/0957-4484/23/23/235601

(90) Zhao, Y.; Jiang, C.; Hu, C.; Dong, Z.; Xue, J.; Meng, Y.; Zheng, N.; Chen, P.; Qu, L. *ACS Nano* **2013**, *7*, 2406. doi: 10.1021/nn305674a

(91) Meng, Y.; Zhao, Y.; Hu, C.; Cheng, H.; Hu, Y.; Zhang, Z.; Shi, G.; Qu, L. *Adv. Mater.* **2013**, *25*, 2326. doi: 10.1002/adma.201300132

(92) Qu, G.; Cheng, J.; Li, X.; Yuan, D.; Chen, P.; Chen, X.; Wang, B.; Peng, H. *Adv. Mater.* **2016**, *28*, 3646. doi: 10.1002/adma.201600689

(93) Liu, L.; Yu, Y.; Yan, C.; Li, K.; Zheng, Z. *Nat. Commun.* **2015**, *6*, 7260. doi: 10.1038/ncomms8260

(94) Sun, H.; Xie, S.; Li, Y.; Jiang, Y.; Sun, X.; Wang, B.; Peng, H. *Adv. Mater.* **2016**, *28*, 8431. doi: 10.1002/adma.201602987

(95) Yang, Y.; Huang, Q.; Niu, L.; Wang, D.; Yan, C.; She, Y.; Zheng, Z. *Adv. Mater.* **2017**, *29*, 1606679. doi: 10.1002/adma.201606679

(96) Hong, M. S.; Lee, S. H.; Kim , S. W. *Electrochem. Solid-State Lett.* **2002**, *5*, A227. doi: 10.1149/1.1506463

(97) Sun, X.; Zhang, X.; Zhang, H.; Zhang, D.; Ma, Y. *J. Solid State Electrochem.* **2012**, *16*, 2597. doi: 10.1007/s10008-012-1678-7

(98) Khomenko, V.; Raymundo-Piñero, E.; Béguin, F. *J. Power Sources* **2006**, *153*, 183. doi: 10.1016/j.jpowsour.2005.03.210

(99) Peng, C.; Zhang, S.; Zhou, X.; Chen, G. Z. *Energy Environ. Sci.* **2010**, *3*, 1499. doi: 10.1039/c0ee00228c

(100) Dai, Z.; Peng, C.; Chae, J. H.; Ng, K. C.; Chen, G. Z. *Sci. Rep.* **2015**, *5*, 9854. doi: 10.1038/srep09854

(101) Demarconnay, L.; Raymundo-Piñero, E.; Béguin, F. *J. Power Sources* **2011**, *196*, 580. doi: 10.1016/j.jpowsour.2010.06.013

(102) Chae, J. H.; Chen, G. Z. *Electrochim. Acta* **2012**, *86*, 248. doi: 10.1016/j.electacta.2012.07.033

(103) Weng, Z.; Li, F.; Wang, D.-W.; Wen, L.; Cheng, H.-M. *Angew. Chem. Inter. Ed.* **2013**, *52*, 3722. doi: 10.1002/anie.201209259

(104) Wu, Z. S.; Ren, W.; Wang, D. W.; Li, F.; Liu, B.; Cheng, H. M. *ACS Nano* **2010**, *4*, 5835. doi: 10.1021/nn101754k

(105) Fan, Z.; Yan, J.; Wei, T.; Zhi, L.; Ning, G.; Li, T.; Wei, F. *Adv. Funct. Mater.* **2011**, *21*, 2366. doi: 10.1002/adfm.201100058

(106) Zhang, X.; Sun, X.; Chen, Y.; Zhang, D.; Ma, Y. *Mater. Lett.* **2012**, *68*, 336. doi: 10.1016/j.matlet.2011.10.092

(107) Jabeen, N.; Hussain, A.; Xia, Q.; Sun, S.; Zhu, J.; Xia, H. *Adv. Mater.* **2017**, *29*, 1700804. doi: 10.1002/adma.201700804

(108) Xiong, T.; Tan, T. L.; Lu, L.; Lee, W. S. V.; Xue, J. *Adv. Energy Mater.* **2018**, *8*, 1702630. doi: 10.1002/aenm.201702630

(109) Zuo, W.; Xie, C.; Xu, P.; Li, Y.; Liu, J. *Adv. Mater.* **2017**, *29*, 1703463. doi: 10.1002/adma.201703463

(110) Kong, D.; Ren, W.; Cheng, C.; Wang, Y.; Huang, Z.; Yang, H. Y. *ACS Appl. Mater. Interfaces* **2015**, *7*, 21334. doi: 10.1021/acsami.5b05908

(111) Zhu, Y.; Wu, Z.; Jing, M.; Hou, H.; Yang, Y.; Zhang, Y.; Yang, X.; Song, W.; Jia, X.; Ji, X. *J. Mater. Chem. A* **2015**, *3*, 866. doi: 10.1039/C4TA05507A

(112) Guan, C.; Liu, X.; Ren, W.; Li, X.; Cheng, C.; Wang, J. *Adv. Energy Mater.* **2017**, *7*, 1602391. doi: 10.1002/aenm.201602391

(113) Gao, S.; Sun, Y.; Lei, F.; Liang, L.; Liu, J.; Bi, W.; Pan, B.; Xie, Y. *Angew. Chem. Inter. Ed.* **2014**, *53*, 12789. doi: 10.1002/anie.201407836

(114) Dong, X.; Guo, Z.; Song, Y.; Hou, M.; Wang, J.; Wang, Y.; Xia, Y. *Adv. Funct. Mater.* **2014**, *24*, 3405. doi: 10.1002/adfm.201304001

(115) Lai, F.; Miao, Y.-E.; Zuo, L.; Lu, H.; Huang, Y.; Liu, T. *Small* **2016**, *12*, 3235. doi: 10.1002/smll.201600412

(116) Liu, S.; Zhao, Y.; Zhang, B.; Xia, H.; Zhou, J.; Xie, W.; Li, H. *J. Power Sources* **2018**, *381*, 116. doi: 10.1016/j.jpowsour.2018.02.014

(117) Wang, D.; Nai, J.; Li, H.; Xu, L.; Wang, Y. *Carbon* **2019**, *141*, 40. doi: 10.1016/j.carbon.2018.09.055

(118) Roldán, S.; Blanco, C.; Granda, M.; Menéndez, R.; Santamaría, R. *Angew. Chem. Inter. Ed.* **2011**, *123*, 1737. doi: 10.1002/ange.201006811

(119) Sheng, L.; Jiang, L.; Wei, T.; Liu, Z.; Fan, Z. *Adv. Energy Mater.* **2017**, *7*, 1700668. doi: 10.1002/aenm.201700668

(120) Sheng, L.; Jiang, L.; Wei, T.; Zhou, Q.; Jiang, Y.; Jiang, Z.; Liu, Z.; Fan, Z. *J. Mater. Chem. A* **2018**, *6*, 7649. doi: 10.1039/C8TA01375F

(121) Akinwolemiwa, B,; Peng, C.; Chen, G. Z., *J. Electrochem. Soc.* **2015**, *162* A5054**.** doi: 10.1149/2.0111505jes

(122) Akinwolemiwa, B.; Wei, C. H.; Yang, Q. H.; Yu, L. P.; Xia, L.; Hu, D.; Peng, C.; Chen, G. Z. *J. Electrochem. Soc.* **2018**, *165*, A4067. doi:10.1149/2.0031902jes

(123) Shen, K.; Ding, J.; Yang, S. *Adv. Energy Mater.* **2018**, *8*, 1800408. doi: 10.1002/aenm.201800408

请将 TOC 图片和英文说明语句(阐述文章的**精华内容**，不是图题)放在此处

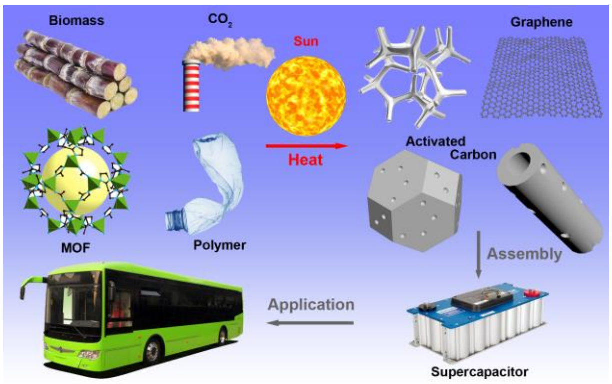

Recent innovations in production of activated carbon and graphene through thermal processing of various new precursors such as biomass, plastic waste and carbon dioxide promise more affordable and sustainable aqueous supercapacitors for a wide range of high power applications, such as electrical buses.